이학박사학위논문

Computational Chemistry Studies on Interfaces: Hydronium/Metal Surface, Electric Double Layer, and Transition Metal Dichalcogenide

계면에 관한 계산화학 연구: 하이드로늄/금속 표면, 전기이중층, 전이금속 다이칼코게나이드에 관하여

2019년 2월

서울대학교 대학원
화학부 물리화학 전공
노 찬 우

Computational Chemistry Studies on Interfaces: Hydronium/Metal Surface, Electric Double Layer, and Transition Metal Dichalcogenide

계면에 관한 계산화학 연구: 하이드로늄/금속 표면, 전기이중층, 전이금속 다이칼코게나이드에 관하여

지도교수 정 연 준

이 논문을 이학박사 학위논문으로 제출함
2019년 1월

서울대학교 대학원
화학부 물리화학 전공
노 찬 우

노찬우의 이학박사 학위논문을 인준함
2018년 12월

위 원 장	석 차 옥	(인)
부위원장	정 연 준	(인)
위 원	이 상 엽	(인)
위 원	신 석 민	(인)
위 원	성 봉 준	(인)

Computational Chemistry Studies on Interfaces: Hydronium/Metal Surface, Electric Double Layer, and Transition Metal Dichalcogenide

by

Chanwoo Noh

Supervised by

Professor **YounJoon Jung**

A Dissertation
Submitted to the Faculty of
Seoul National University
in Partial Fulfillment of
the Requirements for the Degree of
Doctor of Philosophy

February 2019

Department of Chemistry
Graduate School
Seoul National University

Abstract

In this thesis, computer simulations using molecular dynamics and density functional theory were carried out for studying various interfacial systems. The interface is a region where two different substances are adjacent to each other and a chemical reaction takes place. As the size of the material becomes smaller, the role of the interface becomes important. Therefore, it is essential to study the interface in order to understand the microscopic nature of materials. However, experimental studies on interfaces are limited by technical difficulties and can be supplemented by computer simulations. In this thesis, we have studied three kinds of systems in which the role of interface is important: (1) hydronium ions on the platinum surface, (2) an electric double layer capacitor (EDLC), and (3) a two-dimensional transition metal dichalcogenide (TMDC).

In the first chapter, the structure and energetics of the hydronium ion on the platinum(111) surface were studied using the density functional theory. The hydronium ions can be adsorbed on the platinum(111) surface in a multiply hydrated state with neighboring water molecules. It was found that the most important physical quantity for determining the stability of the hydronium ions on the surface is the workfunction of the metal. In addition,

when additional water molecules are adsorbed above the protons, metal-bound protons can migrate to the bulk state through the proton hopping motion along the hydrogen bonding. Combining these results, the Volmer reaction, in which a hydrogen atom is ionized to a hydronium ion, takes place in two-steps, and the metal-bound hydronium ion intermediate plays an important role in an electrochemistry.

In the second chapter, the molecular dynamics is used to investigate the charging phenomenon of the EDLC consisting of 1-ethyl-3methylimidazolium thiocyanate ($[EMIM]^+[SCN]^-$) as an electrolyte. From the ionic layer structure, the differential capacitance was calculated, and the ionic layer structure abruptly changed under the potential condition with the maximum capacitance. The non-equilibrium simulation, which directly simulates the charging process of the EDLC, revealed that the charging dynamics of the EDLC also strongly depends on the transition of the ionic layer. In particular, the amount of the electrode charge during the charging process coincides with the perpendicular displacement of the ionic liquid molecule. From this property, the contribution of each ionic molecule to the electrode charge was analyzed. The charging of the EDLC highly depends on the desorption of the co-ions rather than the adsorption of the counter-ions. It also found that not only the interfacial ionic layer of the EDLC but also the ionic layer in the bulk region plays a significant role in the charging process.

In the last chapter, the orientation and corresponding properties of the two-dimensional TDMC, especially MoS_2 and $PtSe_2$, were studied. First, the growth mechanism in which the direction of MoS_2 synthesized by the chemical vapor deposition (CVD) method is controlled by the thickness of the pre-deposited Mo film was studied through the non-equilibrium MD sim-

ulation. From simulations, we revealed that the internal strain during the growth dictates the orientation of the two-dimensional MoS_2 layers. Next, the electronic band structures of various TMDC layers were calculated. The bandgap structure of the TMDC is highly dependent on the number of stacked layers rather than the individiual detail structure of the layer. Finally, we have found that water molecules can easily bond with the dangling atoms of the TMDC layers. These studies provided new perspectives on the various morphologies of the TMDC layers and their applications.

Keywords: interface, hydronium ions, Pt surface, ionic liquids, electric double layer, electric double layer capacitors, transition dichalcogenide, density functional theory, molecular dynamics

Student Number: 2011-20292

Contents

List of Figures

List of Tables

Chapter 1

Overview

An *interface* is a boundary between two different material or a material in different phases. Since the interface is the boundary at which heterogeneous materials meet, it has special properties which are different from materials in bulk phase: molecular motion on the solid surface can be geometrically constrained, or rapid changes in electrostatic environments may increase the reactivity of molecules. In general, the nature of interfaces is negligible compared to the properties of the bulk state because the ratio of the interface to the volume of material is low. However, the nature of the interface plays a very important role in colloid and nanomaterials where the ratio of surface to particle volume is high, or in heterogeneous catalysts where chemical reactions take place on the surface.[1,2] In addition, as the demand for various electric materials rapidly increases, researches on the interface between charged materials and electrolytes are actively proceeding.[3–6]

Although many interfacial systems are actively researched, the experimental methodologies for the interface are limited due to the constrained environment of material surfaces. Experimental methodologies for the in-

terface include a scanning probe microscopy such as scanning tunneling microscopy (STM) and atomic force microscopy (AFM), or indirect methodologies such as low energy sputtering (LES) and reflection absorption FT-IR spectroscopy (RAIRS).[7–9] They have revealed lots of molecular structures on solid surfaces such as ice layers on metal surfaces, ionic layers near the electrodes, and nanomaterial surfaces, etc. Although lots of experimental studies have discovered the nature of the interfacial systems, there is still a limitation of the need for extreme conditions such as ultra-high vacuum conditions or low temperature.

Computational chemistry, a branch of chemistry that uses computers to reveal chemical reactions and molecular behaviors, can be used to overcome the limitation of experiments on interfaces. With the rapid development of computing power and theoretical methodology, computational chemistry has been used in various systems ranging from simple chemical reactions of small molecules to topological properties of high molecular weight polymers. In order to describe the characteristics of the system adequately, an appropriate methodology should be used. Among various methodologies, density functional theory (DFT) and molecular dynamics (MD) methods are the most widely used in various systems. The DFT method is a quantum mechanical method for quantitatively calculating the electronic structure and energy of a molecule. This method describes the electronic structure of a molecule through the electron density rather than electron orbitals, so it allows precise quantum mechanical calculations for systems containing hundreds of atoms. In contrast, the MD method, one of the empirical methodologies, describes molecules through pre-empirically calculated force-field parameters. Since computation is performed through the already calculated

parameters, it is inaccurate as compared with the DFT methodology. This method, however, has the advantage that it can describe a system containing more than million atoms and can consider the dynamics of molecules.

In this thesis, DFT and MD methods are used to evaluate the molecular and electronic behaviors of several systems in which the interfacial properties are important. The systems used in this thesis are (1) The interface between hydronium/water and platinum, (2) the electric double layer capacitor consisting of an ionic liquid, (3) two-dimensional transition metal dichalcogenide layers.

1.1 Hydronium Ions on the Platinum Surface

In Chapter 2, we study the nature of hydronium ions on the Pt(111) surface by conducting the DFT calculation in a periodic condition. Our computational study is based on the spectroscopic experimental studies in an ultra-high vacuum condition, which suggest the existence of the hydrated protons on the Pt(111) surface.[1,10] We first demonstrate that the protons on the Pt(111) surface can only be present in the multiply hydrated forms by evaluating the energies and the charge distribution of the system. The workfunction of the metal is a significant physical quantity determining the stability of the hydronium ions on the metal interface. Because of the high workfunction of Pt(111) surface, the hydrated protons are able to be an adsorbed state.

In addition, the proton structures in the water monolayer on the metal surface are investigated. Within the metal-bound water monolayer, protons exist in the form of $H_5O_2^+$ or $H_9O_4^+$, which distinguish from hydronium

structures in bulk. If the additional water overlayer is adsorbed on the proton, the proton spontaneously migrated to the bulk phase through the proton hopping mechanism. During the proton migration to the bulk phase, proton rotation must be involved in order to form a hydrogen bonding between a proton and overlayer water molecules. Combining the results of the stability of metal-bound hydronium ions and the spontaneous proton migration to the bulk phase, we suggest the two-stepwise Volmer reaction mechanism. In the suggested mechanism, a metal-bound hydronium ion is produced as an intermediate, and it plays an important role in electrochemistry.

1.2 Electric Double Layer Capacitors

In Chapter 3, we investigate the charging phenomena of the electric double layer capacitor (EDLC) by conducting both the equilibrium and non-equilibrium MD simulations. The 1-ethyl-3-methyl imidazolium thiocyanate ($[EMIM]^+[SCN]^-$) ionic liquid is used as an electrolyte, and two parallel graphene sheets are used as the electrodes. The charged state of the electrode is regulated by the constant potential method, in which the electrode charge is allowed to fluctuate according to the external potential and electrostatic environments. Because the charge distribution in ionic liquids is significantly dense, the electrode charge is highly dependent on the interfacial ion structure. Thus, it is necessary to consider the electrode charge fluctuation in studying the charging behavior of the ionic liquid EDLC.

From equilibrium simulations, the layer structure of $[EMIM]^+[SCN]^-$ ions are analyzed by considering both the distance from the electrode and

the orientation of the ions. The Ionic layer in a discharged state is highly ordered due to their parallel orientation with respect to the electrodes, and the orientational rearrangement should occur during the charging of the EDLC. In addition, the differential capcitance of the EDLC can be calculated from the ionic layer structure. It turns out that the differential capcitance behavior is highly correlated with the rearrangement of the ionic layer structure.

Non-equilibrium charging simulations reveal that the charging of the ionic liquid EDLC occurs in multi-stepwise due to the hierarchical dynamics of the ionic liquids. The charging dynamics is highly dependent on the relaxation of the ionic layer structures. Particularly, the electrode charge during the charging process is consistent with the perpendicular displacement of ionic liquid molecules. Using this property, we analyze the contribution of each molecular ion to the electrode charge stored during charging. Charging of the EDLC is largely dependent on the desorption of the co-ions from the electrode rather than the adsorption of the counter-ions. In addition, the contribution of bulk ions to the charge stored in the EDLC is as important as that of ions adjacent to the electrode surface, which is contrary to the conventional viewpoint. Our findings in the present study are expected to play an important role in designing an efficient EDLC with a novel perspective on the charging of the EDLC.

1.3 Transition Metal Dichalcogenide

In Chapter 4, we study the orientation of the transition metal dichalcogenide (TMDC) and its effect on the physical properties. First, the growth mechanism in which the direction of MoS_2 synthesized by the chemical vapor

deposition (CVD) method is controlled by the thickness of the pre-deposited Mo film is studied through the non-equilibrium MD simulation. In order to simulate the CVD synthesis process of MoS_2, the external strain is imposed on the MoS_2 layers by reducing the simulation box size. From simulations, we reveal that the deformed 2D MoS_2 multilayers do not suffer from the weakening of van der Waals interaction across their basal planes once they are formed. In addition, the multi-layered MoS_2 layers rotate in the vertical direction to resolve the lateral strain applied to them, but monolayers release the mechanical strain by sliding over each other layer. Combining these results, we reveal that the internal strain during the growth of 2D TMDC layers dictates the morphology of the layers. Next, the electronic band structures of 2D TMDC layers in various morphologies are calculated using DFT method. We find out that the band structures are highly dependent on the number of stacked layers rather than the edge structure or the length of the layers. Finally, we reveal that the water molecules are apt to adsorb on the dangling atoms of the TMDCs edge structure. We expect that these consecutive studies provide new insights to understand better various morphologies of 2D TMDC layers and their applications.

Chapter 2.
Hydronium Ions on the Platinum Surface

Chapter 2

Hydronium Ions on the Platinum Surface

2.1 Introduction

Hydronium ions play an important role in a wide variety of chemical phenomena in acidic aqueous environments, and understanding the nature of hydronium ions has been the subject of intense research in physical chemistry. The hydronium ion may be produced by the ionization of an acidic molecules, but it also can be reversibly produced by a heterogeneous reaction of an adsorbed hydrogen at the water/metal interace through a so-called Volmer reaction [eqn. (2.1)].[11]

$$H_{ads} + H_2O \rightleftharpoons H_3O^+ + e^-_{metal} \tag{2.1}$$

This reaction is significant because it is not only a hydronium generating reaction but also a key mechanistic step in water electrolysis and the hydrogen evolution reaction. However, the fundamental mechanism of this process is not well understood: It is not exactly revealed whether the ionization of a H atom to a H_3O^+ ion occurs directly on the metal surface or in the interfacial

solution phase. To answer this question, the exact structure and energetics of the hydronium ions on the metal surface must be identified. However, the nature of hydrated protons formed at electrode/electrolyte interfaces has remained unclear, mainly because of experimental difficulties in probing the electrode/electrolyte interfaces and identifying the hydrated protons with currently available experimental techniques. Although several experimental studies have discovered the nature of the interface between metal and hydronium, there is still a limit of the need for extreme conditions such as ultra-high vacuum conditions or low temperature.[1,2] Therefore, computational methods have been used as alternatives for such interfacial studies.

With fast developments of computational power and concurrent progresses in theoretical methodologies, electrochemical theories utilizing quantum chemical calculations progressively play an important role in revealing microscopic mechanisms in elementary electrochemical reactions occuring on metal surfaces. Among these works, Nørskov and coworkers[12–14] have conducted electron/proton transfer studies through the reaction of partially charged protons by adding neutral hydrogens in water layers on metal surfaces. Through these studies, they found a correlation between the activation energies of the electron transfer reaction and the electrode potential, and proposed a principle for designing improved catalysts using DFT calculations. On the other hand, Schmickler and cowokers have developed the electron transfer theory by introducing the solvent coordinate as the reaction coordinate for reactions.[15–17] From this theory, the free energy surface for an electrochemical reaction can be calculated, and in particular, the reactivity of catalyst can be predicted by measuring the free energy change of proton adsorption on the metal surface. In addition, molecular

dynamics simulation studies of proton transfer on metal surfaces have been carried out, and one of them suggests that weakly adsorbed hydrogens on the Pt(111) surface is in dynamical equilibrium with protons in water.[18] Also, other studies discovered that Grotthuss type proton hopping from bulk to the surface water layer enhances the proton transfer reaction on the Pt surface. Especially, when charge density on the Pt surface is low, Zundel type ions were observed to form transiently at the electrode surface before ions are discharged.[19,20]

Although the aforementioned studies of hydrated protons formed by hydrogen and water adsorption on metal surfaces, a further study is necessary to better understand the nature of hydrated protons on metal surfaces. In particular, it is desirable to examine the properties of surface hydrated protons under conditions that more closely resemble those of an electrode/electrolyte interfaces. In this study, density functional theory (DFT) calculations are performed to understand the structure and energetics of hydrated protons on the Pt(111) surface. From the present study, we clarified the results of spectroscopic experiments, which suggest the existence of the hydronium ions on the Pt(111) surface.[1,10] The rest of the present Chapter is organized as follows. section 2.2 presents the brief description of the system and the DFT calculation methods used in this study. In section 2.3, hydrated proton structures on the Pt(111) surface and their migration to bulk will be discussed. Finally, conclusions will be given at section 2.4.

2.2 Calculation Methods and Models

2.2.1 Structure of hydronium on the Pt(111) surface

Periodic DFT calculations were performed using the Quickstep module[21] of the CP2K program package,[22] which is optimized to perform DFT calculations on periodic systems. Interactions with the frozen cores were described with norm-conserving pseudopotentials, while valence electrons were treated explicitly. For H, O, and Pt atoms, 1, 6, and 18 electrons were used for the valence shell, respectively, and a DZVP basis set was adopted for describing wave functions. A Perdew–Burke–Ernzerhof (PBE) functional,[23,24] which is a kind of the generalized gradient approximation (GGA) potential, was used to describe the exchange-correlation potential. In addition, the DFT-d3 correction was used to describe the van der Waals interactions.[25] The energy cutoff of the electron density was set to 500 Ry and the relative cutoff to 50 Ry. During the calculations, we used the Fermi–Dirac smearing option with a width of 300 K to accelerate convergence of the calculations. In these calculation conditions, the lattice parameter of Pt was optimized to be 3.95 Å. The Pt(111) surfaces were simulated with a slab of four atomic layers containing 6×6 Pt atoms per layer, and water and hydronium ions were adsorbed on the top side of the platinum surface. A periodic boundary condition in the xyz direction was applied to describe the system. To reduce the effect of periodic images of the slab, a vacuum of $\sim 6\ d_s$, where d_s is the slab thickness, was inserted in the simulation box. Only the two bottom layers of the slab were fixed, whereas the two top layers of the slab were allowed to relax during geometry optimization. Geometry optimization was performed using an L-BFGS optimizer.[26] The total charge of the system

was set to be zero. Vibrational normal modes were calculated by diagonalizing the Hessian matrices. If we apply the harmonic approximation to the Hessian, the eigenvector and eigenvalue of the Hessian is the normal modes motion and frequencies respectively. When calculating the Hessian, all platinum atoms were fixed at the optimized configurations. The intensity of each normal mode was calculated as the square of the derivative of the vertical dipole moment.

2.2.2 Ionization energy of hydrated hydrogens

Ionization energy (I.E.) is the required energy when molecules in the gaseous state lose one electron to become cations, which can be defined as following equation,

$$X(g) + \text{I.E.} \rightarrow X^{+}(g) + \text{e}^{-}. \tag{2.2}$$

There are two major methods to calculate the I.E. using DFT calculation. (1) calculating the highest occupied molecular orbital energy of the molecule, and (2) directly calculating the energy difference between neutral state and the cation state. Among these two methods, the I.E. of the multiply hydrated hydrogen was calculated via latter method. Geometry optimization and the energy evaluation of gaseous hydrated hydrogens and their cations were conducted by DFT calculation using GAMESS program.[27] The B3LYP functional was used to describe the exchange functional,[28,29] and orbitals were described with the 6-311G**(d,p) basis sets.

2.2.3 Workfunction of the Pt(111) surface

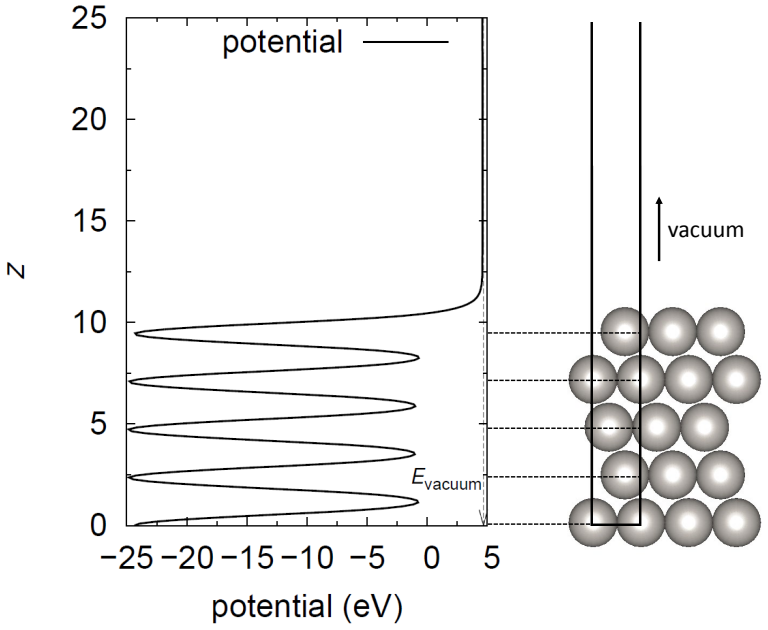

Figure 2.1: Graphical description of local potential and Pt layer structure.

The workfunction of metal (ϕ_{metal}) is the minimum thermodynamic energy required to remove an electron from a metal surface to a vacuum. ϕ_{metal} can be defined as following equation,

$$\phi_{\mathrm{metal}} = E_{\mathrm{vacuum}} - E_{\mathrm{F}}, \tag{2.3}$$

where E_{vacuum} is the electrostatic potential in the vacuum, and E_{F} is the Fermi energy of the metal. The workfunction of the Pt(111) surface is calculated using the Vienna Ab initio Simulation Package (VASP).[30] Wave func-

tions were approximated with projector augmented wave (PAW) pseudopotentials[31] and the Perdew-Burke-Ernzerhof (PBE) functional is used for the exchange-correlation functional.[23,24] Both lattice constant and the atomic positions were optimized until the energy convergence satisfies the criterion of 1.0×10^{-6} eV/Å with a cutoff energy of 500 eV. The reciprocal space was sampled with the Monkhorst-Pack grid of $9 \times 9 \times 1$ k points in the first Brillouin zone of the unit cell. The Pt(111) surface was simulated with the five atomic layers, and it was confirmed that five layers were sufficient to evaluate the workfunction. In these calculation conditions, the lattice constant of Pt crystal was optimized as 3.88 Å. E_{vacuum} was calculated as the plateau value of local potential in z direction, as depicted in Figure 2.1.

2.3 Results and Discussion

2.3.1 Hydronium on the Pt(111) surface

We conducted DFT calculations to elucidate the structures of stable surface hydrated protons. First, we optimized the structure of an isolated hydronium ion on a Pt(111) surface, as depicted in Figure 2.2 (a). Upon approaching from the gas phase onto the surface, the hydronium ion dissociates into a hydrogen atom and a water molecule. The corresponding OH bond length between the oxygen and the hydrogen adjacent to the platinum surface is 1.82 Å, which is longer than the OH bond length of hydronium ions in the gas phase. This larger distance between oxygen and hydrogen denotes that the hydronium ion cannot be stabilized on the platinum surface by itself. However, on adding extra water molecules to the hydronium ion sequentially, as shown in Figure 2.2 (b)–(d), multiply hydrated proton clusters can be stabilized. The stabilized $H_5O_2^+$, $H_7O_3^+$, and $H_9O_4^+$ species have partial charges of +0.69, 0.72, and 0.74, respectively, and Pt atoms have the opposite charges due to the charge neutrality of the system.

Here, atomic charges were calculated by Mulliken charge method. Hirshfeld method also produced a similar result. The partial positive charges on the multiply hydrated protons indicate that they are present in ionic forms, rather than as neutral molecules. Previous DFT calclations have revealed that protons on metal surfaces have partial charges.[12,13,15] For clarity, atomic coordintates and atomic charge data are provided in the Table 2.3-2.6. The bonding interaction between hydrated protons and Pt surface was investigated by calculating the electron density difference, defined as $\Delta\rho(\mathbf{r}) = \rho_{\mathrm{full}}(\mathbf{r}) - [\rho_{\mathrm{Pt}}(\mathbf{r}) + \rho_{\mathrm{ion}}(\mathbf{r})]$, where $\rho_{\mathrm{full}}(\mathbf{r})$, $\rho_{\mathrm{Pt}}(\mathbf{r})$, and $\rho_{\mathrm{ion}}(\mathbf{r})$ are

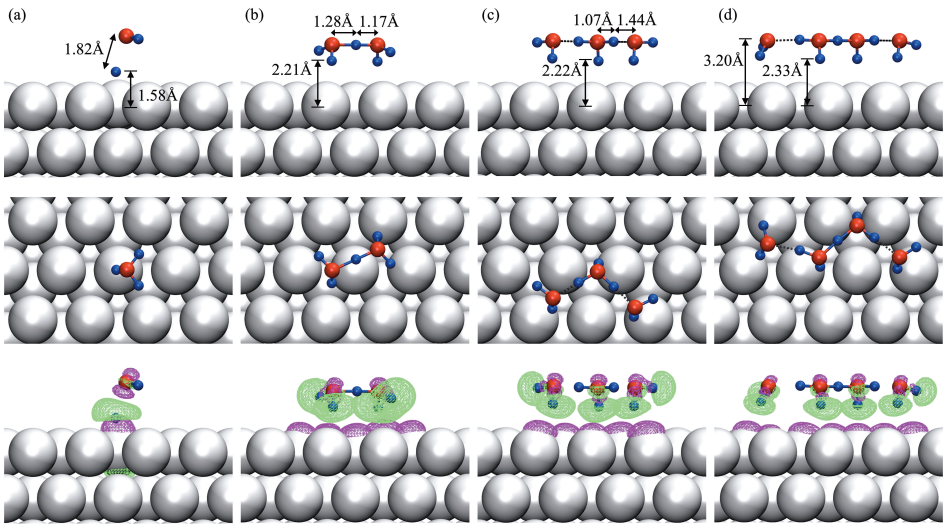

Figure 2.2: Hydronium and multiply hydrated proton species on a Pt(111) surface. The total charge of the system was set to zero. (a) Optimized structure of H_3O^+ on the surface. The distance between oxygen and the proton next to Pt is 1.82 Å. The divided hydrogen and water structure is more stable than H_3O^+. (b) Optimized structure of $H_5O_2{}^+$ on the surface. The proton is shared by two water molecules. (c) Optimized structure of $H_7O_3{}^+$ on the surface. H_3O^+ is stabilized by forming hydrogen bonds with two adjacent water molecules. (d) Optimized structure of $H_9O_4{}^+$ on the surface. Lower panel demonstrates $\Delta\rho(r)$ of each configuration. Here, purple iso-surfaces are negative charge surface, and green ones are positive charge's surfaces. The charge iso-values are $\pm 0.002\ e\text{Å}^{-3}$

the electron densities of the full system, Pt slab, and ions, respectively. As shown in the lower panel of Figure 2.2, the electron density between the water molecule and the hydrogen of the singly hydrated proton is significantly reduced. In contrast, electrons near the hydrogen of the multiply hydrated proton tend to be shifted towards the space between the Pt surface and ion. This enhancement of electron density in the interfacial region evidences the formation of the adsorption bond of the multiply hydrated proton to the Pt surface. The vertical distance between the oxygens of $H_5O_2{}^+$, $H_7O_3{}^+$, and $H_9O_4{}^+$ and the Pt surface is about 3.2 Å, which is similar to the vertical distance between Pt and O atoms of water in a $\sqrt{3} \times \sqrt{3}\ R30°$ (R3) bilayer. The electron distributions and the atomic positions indicate that the multiply hydrated protons are specifically adsorbed on the Pt surface.

In addition to the optimized structures of hydrated proton clusters, the protonation energies, $E_{\text{proto}}(n) \equiv E_{\text{ion}}(n) - E_{\text{water-H}}(n)$, were calculated. Here, $E_{\text{ion}}(n)$ is the energy of hydrated protons of the form $(H_2O)_nH^+$ on the Pt(111) surface, and $E_{\text{water-H}}(n)$ is the energy of co-adsorbed water molecules and a hydrogen atom of the form nH_2O + H on the Pt(111) surface. From the calculations, we obtained $E_{\text{proto}}(1) = 0.69$ eV, $E_{\text{proto}}(2) = -0.30$ eV, $E_{\text{proto}}(3) = -0.18$ eV, and $E_{\text{proto}}(4) = -0.42$ eV. $E_{\text{proto}}(1)$ was approximately obtained as the stabilization energy when a singly hydrated proton, which is not able to be stabilized on the platinum surface, dissociates into a hydrogen atom and a water molecule. The negative values of E_{proto} for $n = 2 \sim 4$ indicate that hydronium ions can be stabilized with just one extra water molecule on the platinum surface. This finding is consistent with the low energy sputtering experimental results,[1,10] which indicate that the major protonated water clusters on the Pt(111) surface are $H_5O_2{}^+$, $H_7O_3{}^+$,

and $H_9O_4{}^+$.

The stability of the multiply hydrated protons on the metal surface can be approximately estimated via the competition between the ionization energy (I.E.) of the hydrated hydrogens and the workfunction of metal surface (ϕ_{metal}). If the adsorption energies of the hydrated hydrogens are neglected, the electron transfer energy of hydrated protons on the metal can be approximately calculated by I.E. $-\ \phi_{\text{metal}}$ as the following equation.

$$\begin{array}{ll} \mathrm{H(H_2O)}_{n,\text{ads}} \rightarrow \mathrm{H(H_2O)}^+_{n,\text{ads}} + \mathrm{e}^- & \Delta E \approx \text{I.E.} \\ + \quad \text{metal} + \mathrm{e}^- \rightarrow \text{metal}^- & \Delta E = -\phi_{\text{metal}} \\ \hline \mathrm{H(H_2O)}_{n,\text{ads}} + \text{metal} \rightarrow \mathrm{H(H_2O)}^+_{n,\text{ads}} + \text{metal}^- & \Delta E \approx \text{I.E.} - \phi_{\text{metal}} \end{array} \tag{2.4}$$

According to eqn. (2.4), hydrated protons on the metal are energetically favorable if the ionization energy of the hydrated hydrogen is smaller than the workfunction of the metal. The ionization energies of the hydrated hydrogens and the workfunction of the Pt(111) surface were calculated following the methods in section 2.2. The workfunction of the Pt(111) surface is calculated as 5.53 eV, and the calcaulated ionization energies of hydrated hydrogens are tabulated in Table 2.1. As the number of hydrated water molecules

Table 2.1: Ionization energies of hydrated hydrogens (units: eV)

Molecular reactions	Ionization energy
$\mathrm{H(H_2O)_1} \rightarrow \mathrm{H(H_2O)_1}^+ + \mathrm{e}^-$	6.17
$\mathrm{H(H_2O)_2} \rightarrow \mathrm{H(H_2O)_2}^+ + \mathrm{e}^-$	4.43
$\mathrm{H(H_2O)_3} \rightarrow \mathrm{H(H_2O)_3}^+ + \mathrm{e}^-$	3.81
$\mathrm{H(H_2O)_4} \rightarrow \mathrm{H(H_2O)_4}^+ + \mathrm{e}^-$	3.56

increases, the I.E. decreases because positive charges can be broadly diffused over the larger cations and they can be stabilized. Interestingly, the I.E. of all multiply hydrated hydrogens except for the singly hydrated hydrogen have values greater than the workfunction of the Pt(111) surface. Since the workfunction of the Pt(111) surface is at an exquisite boundary discriminating the ionization energies of hydrated hydrogens, it induces the phenomenon that only the multiply hydrated protons are stable on the Pt(111) surface. The argument that the workfunction of a metal is a key physical quantity that determines the stability of hydrated protons is supported by previous experimental studies:[10,32] (1) Hydronium ions are not observed on the Cu(110) surface where the workfunction is smaller than Pt(111) surface. (2) When sodium is adsorbed on the Pt(111) surface, hydronium ions become unstable due to the decreased workfunction. Thus, regulating the workfunction of the metal surface is important for the stability of the hydrated protons on the metal surface.

2.3.2 Hydronium-water monolayer on the Pt(111) surface

In addition to the aforementioned calculations for $H_5O_2^+$, $H_7O_3^+$, and $H_9O_4^+$ ions, the optimized structure for hydrated protons in a water monolayer on the Pt(111) surface was determined. In the previous study, it was proposed that a water layer on a hydrogen-adsorbed Pt(111) surface prefers $\sqrt{3} \times \sqrt{3}\ R30^\circ$ (R3) structures.[33] Therefore, we optimized the proton-containing water monolayer structure generated by adding an additional hydrogen atom to the water molecule orienting parallel to the Pt surface in the R3 water monolayer. Although other water layer structures $[(\sqrt{37} \times \sqrt{37}) - R25.3^\circ$ or $(\sqrt{39} \times \sqrt{39}) - R16.1^\circ]$ are also possible for water

monolayers on platinum,[34] proton hydration in these structures seems to resemble that in the R3 monolayer. Thus, the structure estimated from the R3 layer seems adequate for an initial configuration to be optimized. Using DFT optimization calculations, as described in section 2.2, we obtained an optimized proton hydration structure in a water monolayer, as presented in Figure 2.3(a). The hydronium ion is stabilized on the metal surface by forming the $H_7O_3^+$ structure with adjacent water molecules. The hydrogen bond length between the hydronium ion and the water molecule (~ 1.43 Å) is significantly shorter than that between water molecules (~ 1.8 Å). In addition, the distance between the hydronium oxygen and the hydrogen atom of the adjacent water molecule is 2.43 Å, which is much longer than the usual hydrogen bond length. This finding indicates that the oxygen atom of the hydronium ion is not able to form a hydrogen bond with hydrogen atoms of water molecules. Thus, the hydronium ion is tightly bound to two adjacent water molecules to form $H_7O_3^+$. Hereafter, this hydrated proton in water monolayer structure in Figure 2.3(a) is referred to as a metal bound (MB)-$H_7O_3^+$ layer.

Figure 2.3 (b) shows another possible proton hydration structure in the water monolayer, which is termed a MB-$H_9O_4^+$ layer. The MB-$H_9O_4^+$ structure is 0.44 eV more stable than the MB-$H_7O_3^+$ structure. This energy difference involves the structural changes of 24 water molecules in the unit cell as well as hydronium itself, so this difference is not very large. The MB-$H_9O_4^+$ layer can be generated from a MB-$H_7O_3^+$ layer via two sequential proton-hopping processes without any molecular rotation. Accordingly, the energy barrier between these two structures will be very small or absent, and the transition between these two structures seems to occur frequently.

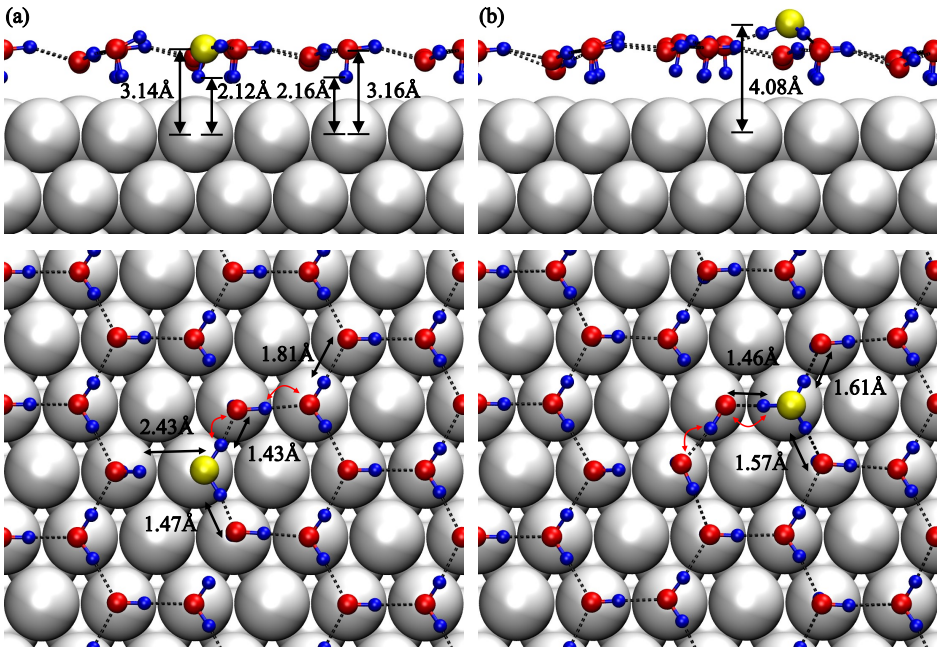

Figure 2.3: (a) Proton hydration structure in an adsorbed water monolayer on a Pt(111) surface. The structure is optimized from the $\sqrt{3} \times \sqrt{3}$ water monolayer. The hydronium ion is highlighted as a yellow sphere. The hydronium ion exists as $H_7O_3{}^+$ directly bound to the metal surface, which is named the MB-$H_7O_3{}^+$ structure. (b) Another structure for proton hydration in the water monolayer. The hydronium ion exists as $H_9O_4{}^+$ bound to water molecules, which is named the MB-$H_9O_4{}^+$ structure. Transitions between the MB-$H_7O_3{}^+$ and MB-$H_9O_4{}^+$ structures occur easily by proton hopping as depicted in red curved arrows.

In the MB-$H_9O_4^+$ structure, the hydronium ion forms a $H_9O_4^+$ structure with three water molecules, and the hydrogen bond between water and the hydronium ion is stronger than that between water molecules. However, the hydronium in the MB-$H_9O_4^+$ structure is different from the Eigen complex in the bulk state, which has a three-dimensional structure with H_3O^+ bonded to three neighboring water molecules. In the case of the MB layer, the two-dimensional hydrogen bonding network hinders the development of bulk-state $H_3O(H_2O)_3^+$ and restrains possible configurations of the MB layer. These restrictions lead to the formation of two-dimensional MB-$H_7O_3^+$ and MB-$H_9O_4^+$ structures. These two MB structures are also similar to the H_3O^+ down and H_3O^+ planar structures found in the work of Nørskov group.[12] Although MB-$H_9O_4^+$ is a global minimum structure in DFT calculations of the water monolayer system, both MB-$H_9O_4^+$ and MB-$H_7O_3^+$ structures may coexist in a water monolayer because of rapid interconversion via proton transfer, as illustrated in Figure 2.3.

2.3.3 Migration of protons from surface to bulk

The transformation of MB hydrated protons into three-dimensional structures in the water multilayer was investigated. Several model structures for the water overlayer were generated by adding a few water molecules onto the MB-$H_7O_3^+$ and MB-$H_9O_4^+$ layers. Geometry optimization of these structures revealed that the hydrated proton migrates to the second layer when at least four water molecules are added onto the hydronium-water monolayers. Figure 2.4 shows various configurations of the MB-$H_7O_3^+$ and MB-$H_9O_4^+$ layers with four water molecules during geometry optimization. Although the L-BFGS optimization method may not reproduce the

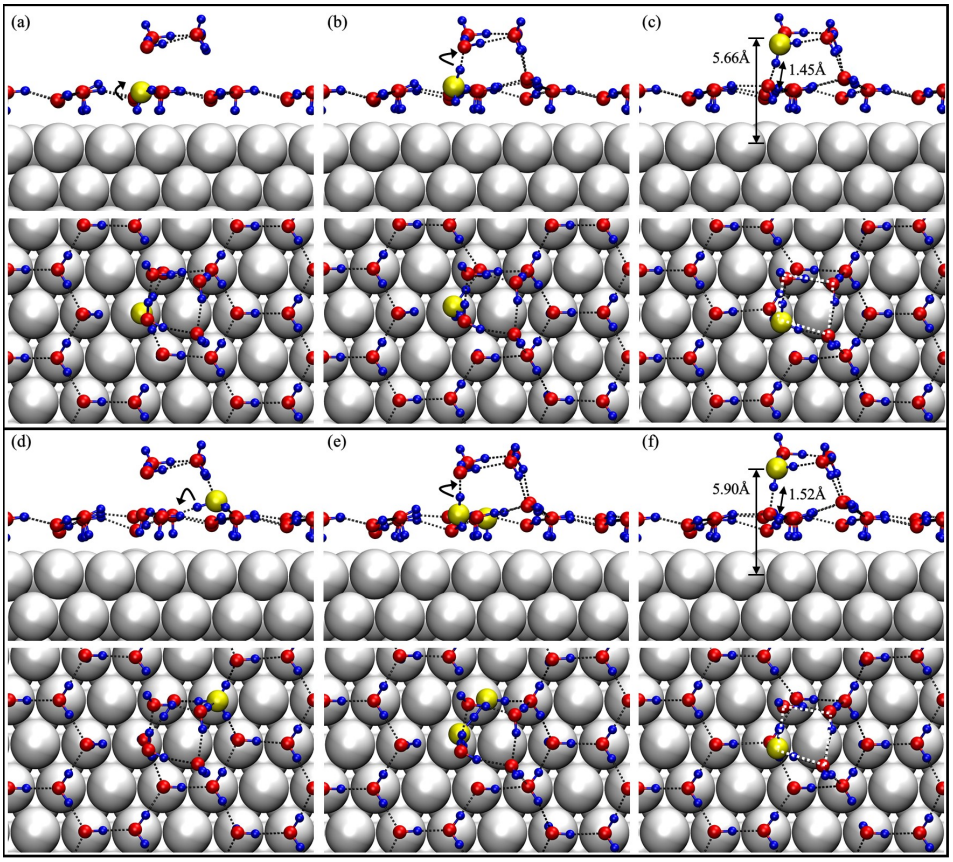

Figure 2.4: Configurations of MB-$H_7O_3^+$ ((a), (b), (c), upper panel) and MB-$H_9O_4^+$ layers ((d), (e), (f) lower panel) with four adsorbed water molecules during geometry optimization. (a), (d) Initial configurations generated by adding four water molecules above a hydronium ion in the MB layers. (b), (e) During the optimization process, the hydronium ion rotates and forms a hydrogen bond with a water molecule in the upper layer. (c), (f) Optimized structures of the MB layers with four water molecules.

real-time dynamics of the system, the configurations obtained during the optimization process suggest a possible reaction pathway. First, upon optimizing the structure, the configurations of the hydronium ion and the water molecules change to form as many hydrogen bonds as possible. Second, the metal-bound hydronium ion rotates to form a hydrogen bond with a water molecule in the second layer. Finally, after forming a hydrogen bond between the hydronium ion in the first layer and the water molecule in the second layer, the hydrated proton migrates to the water molecule to form the four-membered hydronium ring structure in the second layer. This hydronium ion above the water monolayer is fully hydrogen bonded with water to form the $H_9O_4^+$ structure. During the proton migration, the energy barrier is very low because a proton hopping motion occurs without seriously destroying the hydrogen bonding network regardless of the initial water layer structures. In addition, it is noteworthy that the proton cannot migrate to the upper layer when three or fewer water molecules are adsorbed on the hydronium. The hydronium ring structure seems to be a key structure for a transformation of a surface hydrated proton to a bulk hydrated form.

We further investigated how the aforementioned hydronium migrated to the second water layer changes when more water is added. In particular, we optimized the structure of two-layer water with a hydronium that was generated by inserting additional water molecules immediately above the water molecules in the configuration of Figure 2.4 (c). The characteristic configurations during optimization are depicted in Figure 2.5. In this two-layer structure, water molecules and the hydronium ion form a hydrogen bond network not only within each layer but also between the two layers, which causes the hydronium ion to exist as a three-dimensional $H_9O_4^+$ ion.

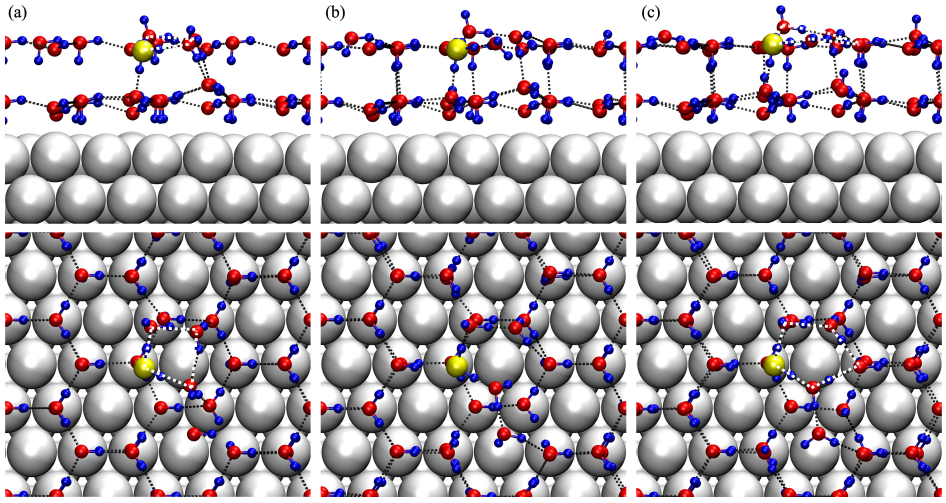

Figure 2.5: Configurations of hydronium and two water layers during the geometry optimization. (a) Initial configuration was generated by inserting additional water molecules to the structure of the Figure 2.4 (c). (b) Water molecules on the second layer form hydrogen bonds with the water on the first layer. (c) Optimized structure. Four membered hydronium ion ring structure is transited to the five membered ring.

Thus, the hydrated proton in the second layer adopts a bulk-state structure. In addition to the dimensionality of the hydrogen bond network, the four-membered hydronium ring structure relaxes into a more stable five-membered ring structure, but the hydronium ion still exists in the second layer. As noted previously, the optimized structure in this calculation is one of many possible structures for a hydronium ion in the water layer, considering the large number of degrees of freedom and thermal fluctuation. However, the fact that the hydronium ion transferred to the second layer does not return to the first monolayer seems robust, indicating that hydronium ions prefer to be located in the second layer rather than embedded in the Pt adsorbed layer.

In order to figure out the difference between the hydronium in the first and the second water layer, the vibrational analysis was applied. Figure 2.6 presents the calculated IR spectra of various hydrated proton structures. Calculated IR spectra is consistent with the experimental reflection absorption infrared spectroscopy (RAIRS) of hydronium/water layers on the Pt(111) surface.[10] The vibrational bands of water are located at 3000–3900 cm^{-1} (O–H stretching), $\sim$ 1600 cm^{-1} (scissoring), and $\sim$ 900 cm^{-1} (librational mode), which agree with the experimental RAIRS bands of a water monolayer.[35] Hydrated protons produce additional features in the regions of 1000–1500 cm^{-1} and 1800–2800 cm^{-1}, which are highlighted as colored regions. The features in the 1000–1500 cm^{-1} region consist of two kinds of vibrations: librational modes of hydronium and its adjacent water molecules, located at 1000–1200 cm^{-1}, and the umbrella mode of hydronium, located around 1400 cm^{-1}. For clarity, the corresponding vibrational frequencies for individual layer structures are listed in Table 2.2, and the vibrational

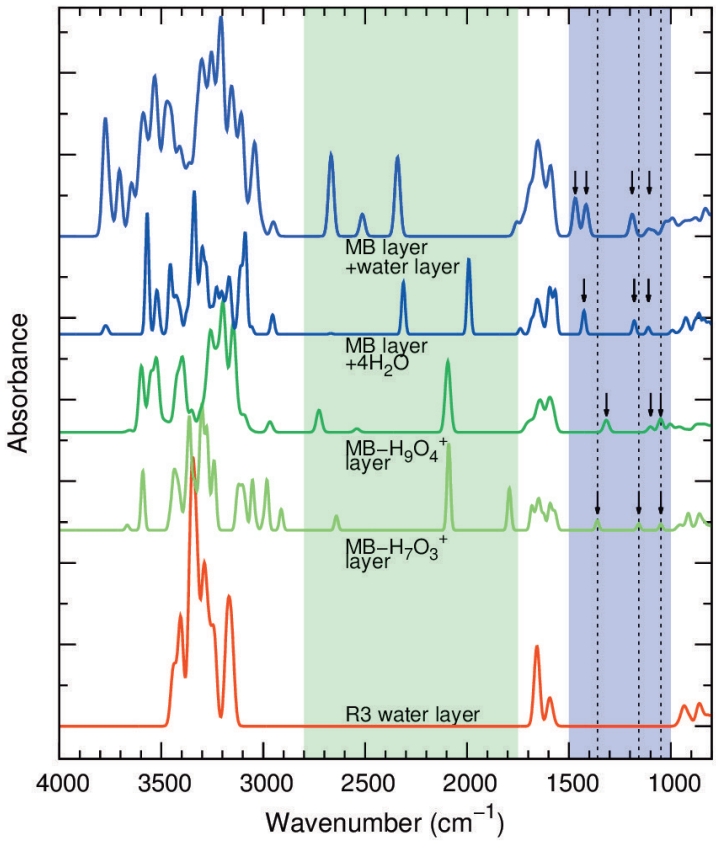

Figure 2.6: Calculated IR spectra of various water layer structures: R3 water layer, MB-$H_7O_3^+$ layer (Figure 2.3 (a)), MB-$H_9O_4^+$ layer (Figure 2.3 (b)), MB-$H_9O_4^+$ layer + $4H_2O$ (Figure 2.4 (c)), and MB-$H_7O_3^+$ +water overlayer (Figure 2.5 (c)). The arrows denote the librational and umbrella modes of the hydronium unit in these structures. The spectral intensities were calculated from the squared derivatives of the dipole moments for the modes perpendicular to the surface, and the spectral width was Gaussian-broadened by 30 cm^{-1}.

motions of hydronium and water molecules are depicted in Figure 2.7. It is noteworthy that the hydronium librational motion involves not only the internal motion of the hydronium ion but also the movement of adjacent water molecules.

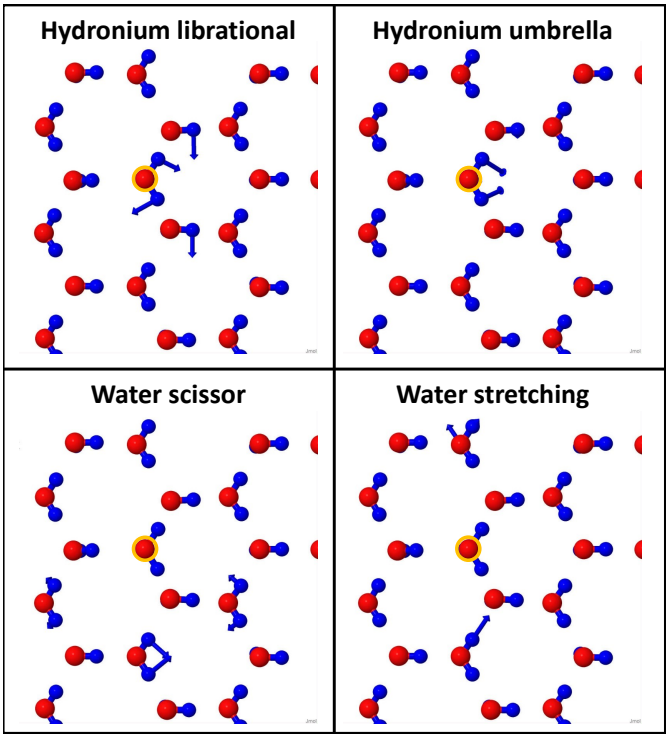

Figure 2.7: Representative vibrational motions of the hydronium and water in the MB-$H_7O_3^+$ layer (Figure 2.3(a)). Oxygens of the hydronium ion are highlighted with orange circles. The platinum is neglected for clarity.

Table 2.2: Vibrational frequencies of normal modes. (units: cm^{-1})

	Figure 2.3(a)	Figure 2.3(b)	Figure 2.4(c)	Figure 2.5(c)
H_3O^+ librational	1049, 1157	1050, 1099	1110,1180	1106,1190
H_3O^+ umbrella	1360	1316	1426	1469
H_2O scissor	1560–1650	1560–1660	1560–1700	1560–1700
H_2O stretching	3000–3600	2900–3600	2900–3600	2900–3900

Focusing on the vibrational features of the hydronium, the frequencies of the librational modes are determined by intermolecular interactions, especially hydrogen bonds. The hydrogen bond between the hydronium ion and a water molecule is stronger than that between water molecules. Therefore, the librational frequencies of hydronium ions, which are located around 1130 cm^{-1}, are blue-shifted with respect to that of pure water (below 1000 cm^{-1}). An important feature of this analysis is that the calculated frequencies of librational vibrations are similar, despite the different hydronium structures in MB-$H_7O_3^+$ and MB-$H_9O_4^+$ layers. This similarity may result from both hydronium structures being bound to the metal. Another important feature is the blue shift of the hydronium-related bands on addition of water molecules. This blue shift is related to a structural change of hydronium ions. In support of this interpretation, the vibrational bands in the 1000–1500 cm^{-1} region do not appear in the spectra of pure water films. The motion of hydronium ion in three-dimension is more constrained than that in two-dimensional networks. Thus, the calculated IR spectra qualitatively indicate the transformation of two-dimensional MB hydronium ions into three-dimensional structures as the water overlayer is developed.

2.3.4 Implications for the Volmer reaction

The stability of multiply hydrated protons on the Pt(111) surface suggests that metal bound hydronium ions can exist on Pt electrode surfaces during the Volmer reaction (Eqn. 2.1). We propose that metal-bound hydronium ions are intermediate species in the Volmer reaction mechanism. As illustrated in Figure 2.8, the first step of the reaction may be ionization of an adsorbed hydrogen atom to a multiply hydrated proton that is specifically adsorbed on the electrode surface, which occurs via electron transfer from the adsorbed atom to the metal. Then, the surface hydrated proton becomes fully solvated as it migrates to the bulk phase. This migration occurs through successive proton-hopping events (Grotthuss mechanism) without translational motions of molecules, which have large energy barriers. The solvated protons in the bulk are enegetically favorable than the surface hydrated protons according to the present results. Therefore, we expect that an analogous process at an electrode/electrolyte interface would also occur spontaneously.

The first step, electron transfer from an adsorbed hydrogen atom to the metal, occurs instantaneously once an appropriate surrounding water structure is formed for electron tunneling. The second step, proton transfer from the adsorbed hydrated proton to water molecules in solution, requires further rearrangement of the proton hydration structure, even in the case of the Grotthuss mechanism. Therefore, the second step will occur with a certain time delay after the first step. As such, the surface hydrated proton is considered a kinetic intermediate state of the Volmer reaction. This interpretation is in contrast to the previous understanding of the ionization

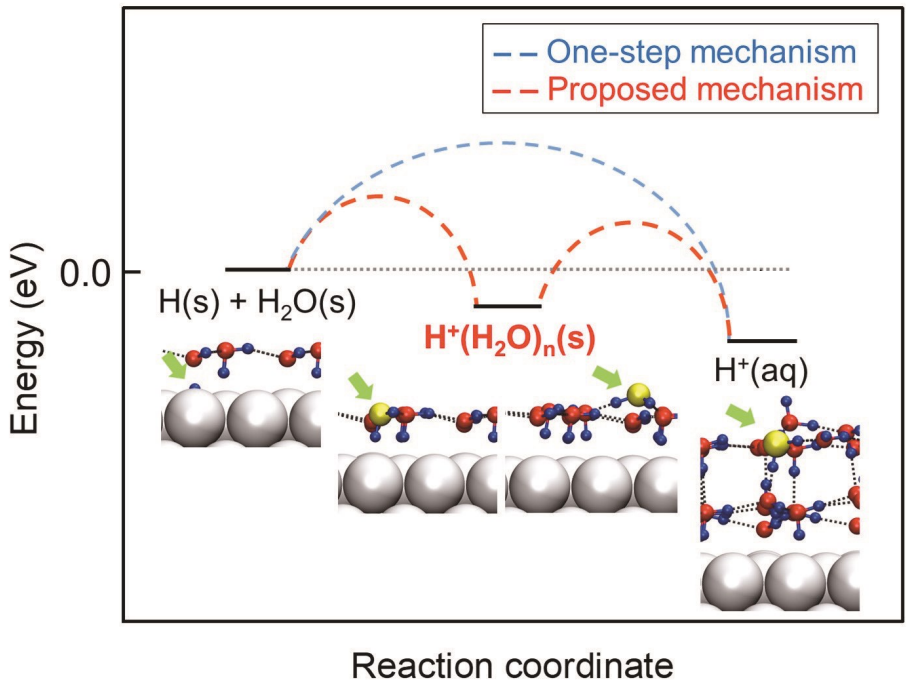

Figure 2.8: Schematic diagram of Volmer reaction.

mechanism, in which the conversion from an adsorbed hydrogen atom to H^+(aq) was considered to occur in a single step. Although the surface adsorbed hydronium in the two-step mechanism is the kinetic intermediate of the Volmer reaction, the surface hydronium plays an important role in electrochemical process on the Pt(111) surface. For example, in the suggested mechanism, hydrated protons can diffuse via a proton hopping mechanism along the surface water layer,[36] which can occur very fast compared to

hydrogen atom diffusion on the metal surface. The proton hopping path may significantly reduce the kinetic constraint of hydrogen diffusion on an electrode surface.

2.4 Conclusions

Examination of various proton strucutures on a Pt(111) surface using DFT calculation revealed that the hydrogen atoms on the Pt(111) surface can be ionized to protons. During the electron transfer, the stabilization of protons through the hydrogen bonding with adjacent water molecules are necessary, so only multiply hydrated proton structures ($H_5O_2^+$, $H_7O_3^+$, and $H_9O_4^+$) are able to present on the Pt(111) surface. $H_5O_2^+$ species may exist on the Pt(111) surface under a condition where water molecules are sparse. However, $H_7O_3^+$ and $H_9O_4^+$ units are major species of the two-dimensional hydronium embedded in the water monolayer on the Pt(111) surface because of the strong hydrogen bonding tendency between the hydronium ion and water molecules. Critical parameters that determine the stability of surface hydrated protons include the ionization energy of hydrated hydrogens and the metal workfunction. By regulating the workfunction, the stability of the protons on the electrode can be controlled.

Addition of a water overlayer on the surface hydrated proton induces the proton migration which reults in fully hydrated, three-dimensional structures. DFT calculations showed spontaneous conversion of metal bound hydrated protons to "nonspecifically adsorbed" $H_9O_4^+$ structures in the presence of added water molecules via proton transfer along the water hydrogen bonds. The migrated $H_9O_4^+$ structure, which resembles the Eigen cation in

bulk water, is different from the metal adsorbed $H_9O_4^+$ structure due to the different hydrogen bonding environment. The stability of hydrated protons in the adsorbed water layer and their migration to bulk phase behavior suggest that the surface hydrated protons may be formed as an intermediate state during the electrochemical Volmer reaction on a Pt(111) electrode. It is anticipated that surface hydrated protons may also be formed on other high workfunction electrode surfaces during electrochemical conversion of hydrogens. The present work demonstrates that computational studies on simplified model systems for electrolyte/electrode interface may provide useful insight into fundamental electrode surface processes.

2.5 Supporting materials

Table 2.3-2.6 show coordinates and atomic charges of various hydrated protons on the Pt(111) surface. The data for Pt atoms are omitted for clarity.

Table 2.3: Coordinates and charge of HH_2O (Figure 2.2 (a))

	x/Å	y/Å	z/Å	Mulliken charge /e	Hirshfeld charge /e
O	10.171	7.285	10.216	-0.335	-0.457
H	9.657	7.274	8.466	0.149	0.280
H	10.766	8.045	10.070	0.218	0.278
H	10.749	6.510	10.081	0.218	0.278
Total charge				0.249	0.379

Table 2.4: Coordinates and charge of $H_5O_2{}^+$ (Figure 2.2 (b))

	x/Å	y/Å	z/Å	Mulliken charge /e	Hirshfeld charge /e
O	5.882	7.225	9.782	-0.290	-0.394
H	5.864	6.600	8.999	0.225	0.283
H	7.052	7.763	9.778	0.301	0.278
H	5.236	7.914	9.496	0.235	0.291
O	8.115	8.250	9.767	-0.245	-0.364
H	8.109	8.890	8.970	0.229	0.289
H	8.740	7.559	9.429	0.239	0.296
Total charge				0.695	0.679

Table 2.5: Coordinates and charge of $H_7O_3^+$ (Figure 2.2 (c))

	x/Å	y/Å	z/Å	Mulliken charge /e	Hirshfeld charge /e
O	8.676	7.157	9.925	-0.263	-0.380
H	9.463	6.432	9.947	0.286	0.273
H	8.727	7.558	9.005	0.220	0.285
H	7.749	6.635	9.958	0.284	0.273
O	10.499	5.419	9.930	-0.354	-0.438
H	10.446	4.979	9.034	0.220	0.274
H	11.385	5.835	9.912	0.229	0.286
O	6.506	5.869	9.990	-0.356	-0.437
H	5.733	6.464	9.914	0.230	0.286
H	6.471	5.360	9.136	0.222	0.273
Total charge				0.718	0.695

Table 2.6: Coordinates and charge of $H_9O_4^+$ (Figure 2.2 (d))

	x/Å	y/Å	z/Å	Mulliken charge /e	Hirshfeld charge /e
O	8.373	7.032	9.999	-0.324	-0.413
H	9.222	6.447	10.018	0.269	0.267
H	8.385	7.475	9.110	0.217	0.276
H	7.423	6.307	10.006	0.304	0.269
O	10.463	5.483	9.997	-0.369	-0.455
H	10.357	4.922	9.188	0.216	0.269
H	11.281	5.983	9.799	0.222	0.279
O	6.514	5.471	9.998	-0.342	-0.424
H	5.556	5.823	10.047	0.268	0.266
H	6.561	5.025	9.112	0.216	0.273
O	3.981	6.135	9.999	-0.372	-0.459
H	3.774	7.044	9.701	0.215	0.277
H	3.614	5.585	9.267	0.218	0.268
Total charge				0.737	0.693

Chapter 3.
Electric Double Layer Capacitors

Chapter 3

Electric Double Layer Capacitors

3.1 Introduction

An electric double layer capacitor (EDLC), or a supercapacitor, is a promising energy storage device with a superb power density and a good energy density.[37,38] Its superior electrical performance arises from the electric double layer (EDL), which is a layer structure formed by adsorbing electrolyte ions with opposite charges on a charged electrode.[39–46] Ions can quickly rearrange themselves in such a way that the electric field generated by the electrode charge can be screened within a subnanometer length scale. In addition, since the EDL structure is not accompanied by any chemical reaction, EDLC has a higher cyclability and a faster charging rate than conventional chemical cells.

In particular, EDLCs using carbon nano-material as an electrode show excellent performance.[47–50] Carbon nano-electrodes maximize the electrode surface area in EDLCs to improve capacity and energy density.[51,52] Among various carbon-nanomaterials, graphene-based materials are promis-

ing candidates for replacing conventional EDLC electrodes. Graphene has remarkable advantages such as a large surface area, a high electrical conductivity, a great mechanical stiffness, and an efficient electrolyte adsorption property.[53,54] In particular, it serves as a prototype for EDLC due to its simple, flat structure. Due to these properties, EDLCs consisting of graphene have been studied in many experiments and computer simulations,[39,47,55–60] and they have shown superior performances compared to conventional capacitors.

In addition to the electrodes, electrolytes also play an important role in determining the performance of the EDLCs. The energy density and the power density of the EDLC are proportional to the square of the operating potential, so increasing the operating potential of the EDLC is important for achieving a high energy and power density of the EDLCs.[37] Generally, the maximum operating potential is limited by the electrochemical window of the electrolytes. Aqueous electrolytes, which are commonly used in the EDLC, have the disadvantage of narrow electrochemical windows within 2 V. To overcome this problem, ionic liquids have been used as an alternative electrolytes in the EDLCs.[61–64] Ionic liquids have advantages of a wide electrochemical windows up to $4 - 5$ V, a low volatility, and a high boiling temperature, so the EDLC can operate in more severe conditions.[65] However, ionic liquids have some drawbacks as well as the aforementioned advantages as the electrolytes of the EDLCs. The conductivities of ionic liquids are lower than conventional electrolytes due to their high viscosity, which may result in a reduced power density. Therefore, it is very important and necessary to understand the dynamical properties of the electric double layer of ionic liquids in order to design EDLCs with desirable properties.

Fundamental theories for EDLs have been developed along with the application of the EDLC. The most basic theory of the EDL is the Helmholtz theory, which describes the EDL as a simple monolayer of counter-ions adsorbed on the electrode. In this theory, however, any space charge of ions behind the first ion layer is not considered.[66] To overcome this limitation, the Gouy-Chapman theory describes the EDL as a diffuse layer with a constant thickness, taking into account thermal fluctuation effects. While being a simple model, the Gouy-Chapman theory can explain the behavior of the EDL of the dilute electrolyte successfully.[67] However, EDLs with a high ion density cannot be described by these simple theories. Recently developed theories based on the Landau-Ginzburg model or the mean-field theory have been successful in explaining the structural aspect of the EDL of ionic liquids.[50,68–70] The ionic liquid EDL described in these theories exhibits an oscillating structure from the electrode due to the *crowding* and *overscreening* effects.

Based on the theoretical development of the EDL of the ionic liquids, its structure has been discovered in various experiments and computational simulations. The ionic density and the thicknesses of ionic layers have been characterized by *in situ* NMR,[71] X-ray spectroscopy,[3,4] and the AFM experiments.[5,6] These experiments revealed that the counter-ions directly contact with the electrode, and the EDL of ionic liquids consists of alternating layers of anions and cations. Combining with the molecular examination of molecular dynamics (MD) simulation studies,[72–76] there have been significant advances in understanding the complex structure of ionic layers in the EDLC. However, most of these studies have focused on the static equilibrium properties of the EDLC, which did not directly examine the

process of charging. Although there are several MD simulation studies of charging,[77–80] in-depth analysis of the ionic layer structure is still desirable. The dynamics of the EDL is directly related with the time-dependent properties in EDLCs, such as power density and the charging/discharging rate. In addition, recent studies have shown that the capacitance of the EDLC is highly correlated with the ionic layer structure of the electrolyte, even 10 Å far away from the electrodes.[57,58] Thus, it is necessary to investigate the evolution of the EDL during the charging in order to fully understand the behavior of the EDLC.

In this chapter, we investigated the charging and discharging dynamics of the EDLC with ionic liquids by conducting the MD simulations under the constant potential condition. We analyzed the motion of ions during the charging process and confirmed the relationship between the charging dynamics and the ionic layer structures. In this work, we focused on 1-ethyl-3-methyl imidazolium thiocyanate ($[EMIM]^+[SCN]^-$), the electrolyte which exhibits the largest capacitance among cyano-based ionic liquids studied in our previous work.[58] It is known that $[EMIM]^+[SCN]^-$ has a sufficiently wide electrochemical window of 3.2 V,[81] and it has the advantages of higher conductivity and lower viscosity at room temperature than more commonly used ionic liquids.[64]

The rest of this Chapter is organized as follows. Background of the EDLC will be given in section 3.2. section 3.3 presents the description of the system and the MD method used in this study. In section 3.4, ionic layer structures in equilibrium state and the charging dynamics of the EDLC are analyzed. Conclusions will be given at section 3.5.

3.2 Theories for Electric Double Layer

An EDL plays an important role in understanding the interface between the charged surface and the ionic liquids. The classical models of the EDL for flat electrodes and ordinary inorganic electrolyte solutions were developed a century ago. Depending on how electrolytes are described, Helmholtz, Gouy-Chapman and Stern models were developed as classical EDL models, as depicted in Figure 3.1. Although these classical models are suitable for ordinary sparse electrolytes, they cannot explain the EDL in high charge density electrolytes such as molten salts or ionic liquids. Mean field theories for the EDL of Ionic liquids were recently developed by Kornyshev and his coworkers.

3.2.1 Classical EDL theories

The earlist model for an EDL was suggested by Helmholtz.[66] The EDL in the Helmholtz model is described as a bilayer consisting of electrode charge and its counter-ions in an electrolyte, as depicted in Figure 3.1. The corresponding single layer of ions totally screens the electrode charge. Because of this bilayer structure in the Helmholtz model, the electrolyte structure near the electrodes is called "electric double layer". The relation between an electrostatic potential and the charge distribution is described by the Poisson's equation,

$$\frac{\partial^2 \Psi(z)}{\partial z^2} = -\frac{4\pi\rho(z)}{\epsilon^*}, \tag{3.1}$$

where $\Psi(z)$ is the electrostatic potential, $\rho(z)$ is the charge density, ϵ^* is the effective dielectric constant of the medium, and z is the distance from the

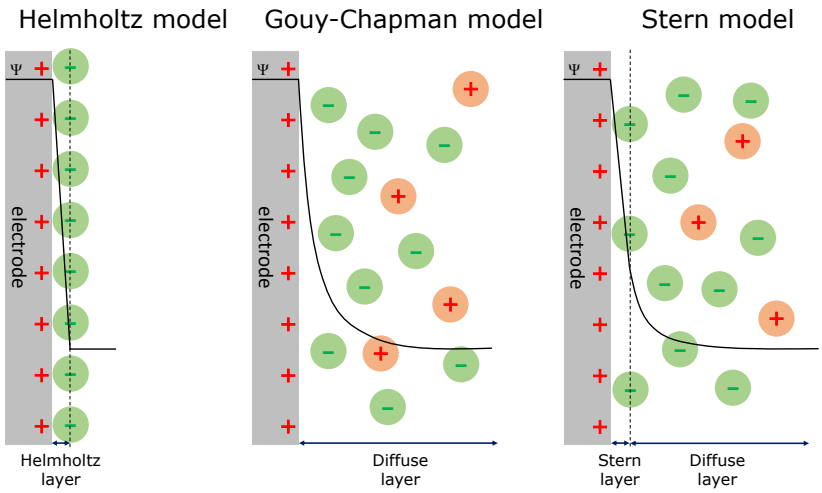

Figure 3.1: Classical models for an electric double layer. From left to right, Helmholtz model, Gouy-Chapman model, and Stern model are depicted. Ψ is the electrostatic potential at the electrode surface, and the black line denote the potential profile.

electrode. Because the charge density between the electrode and electrolyte is zero in the Helmholtz model, the electrostatic potential drops linearly between two layers. Therefore, the capacitance of the Helmholtz EDL is same with that of the macroscopic capacitor, and it is given by

$$C_{\text{Helmholtz}} = \frac{\epsilon^*}{4\pi d}, \tag{3.2}$$

where d is the distance between the electrode and ion layers. Although the Helmholtz theory is quite simple, the estimated capacitance agrees with the order of typically measured capacitance of ordinary electrolytes.

However, the EDL in the real system is not one layer thick structure

due to the thermal fluctuation of the ions. Gouy and Chapman seperately suggest a diffuse layer model which considers the thermal fluctuation of ions by applying the Poisson-Boltzmann differential equation.[82,83] In this model, the charge density is described as Boltzmann equation,

$$\rho(z) = \sum_i c_i \mathrm{e} n_i = \sum_i c_i \mathrm{e} n_i^0 \exp\Big(\frac{-c_i \mathrm{e}\Psi}{k_\mathrm{B}T}\Big), \tag{3.3}$$

where n_i is the number density of i ions, n_i^0 is the bulk number density of i ions, c_i is the charge on the i ion, e is the unit charge, k_B is the Boltzmann constant, and T is the temperature. Combining the eqn. 3.1 and eqn. 3.3, we can obtain Poisson-Boltzmann equation:

$$\frac{\partial^2 \Psi(z)}{\partial z^2} = -\frac{4\pi \mathrm{e}}{\epsilon^*} \sum_i c_i n_i^0 \exp\Big(\frac{-c_i \mathrm{e}\Psi}{k_\mathrm{B}T}\Big). \tag{3.4}$$

By solving the eqn. 3.4, the capacitance of the EDL in the Gouy-Chapman model is derived as following equation,

$$\begin{aligned} \lambda_\mathrm{G} &= \frac{\sqrt{\frac{\epsilon^* k_\mathrm{B} T}{8\pi \mathrm{e}^2 n_i^0}}}{\cosh\Big(\frac{\mathrm{e}\Psi_0}{2k_\mathrm{B}T}\Big)}, \\ C_\mathrm{GCh} &= \frac{\epsilon^*}{4\pi\lambda_\mathrm{G}}. \end{aligned} \tag{3.5}$$

Here, λ_G is the Gouy length, Ψ_0 is the potential at the electrode. In the Gouy-Chapman model, an ionic layer has a finite size of λ_G, and it is successful in predicting the EDL properties in a low potential condition. However, this model is a continuum mean-field model assuming that the ions are point charges in the thermodynamic equilibrium. Especially, the capacitance grows unlimitedly in high Ψ_0 limit, in contradiction to experiments

in which the capacitance always has finite value at large potentials. The failure of the Gouy-Chapman model is due to that it does not consider the finite size of ions and any discreteness at boundary conditions.

In 1924, Stern simply developed the electric double layer theory by introducing a "cutoff", having added a compact Helmholtz capacitance in series to the Gouy-Cahpman capacitance.[84] Thus, the capacitance of the EDL in Stern model can be described by

$$\frac{1}{C_{\text{Stern}}} = \frac{1}{C_{\text{Helmholtz}}} + \frac{1}{C_{\text{GCh}}}. \tag{3.6}$$

The overall potential drop can be split into two parts, the potential decreases linearly within the compact Stern layer, and then decays exponentially in the diffuse layer, as depicted in Figure 3.1. By considering the ion adsorption characteristics at the electrode, classical EDL models have become more sophisticated.

3.2.2 EDL theory for ionic liquids

The series of classical EDL theories could describe the EDL consisting of dilute electrolytes. However, the EDL consisting of an ionic liquid deviates much from these theories. In particular, the differential capacitance of the ionic liquid EDL exhibited a maximum, rather than a minimum, near the potential of zero charge. To overcome this phenomenon, Kornyshev suggested a mean-field lattice gas model describing the EDL of ionic liquids in 2007.[42] In this lattice gas model, N_+ cations and N_- anions, with a fixed total number $\overline{N} = N_+ + N_-$, are distributed over N lattice sites. The electrostatic potential Ψ of the system is self-consistently determined by the ion densities near the boundary with the electrode. The free energy of such

system was approximated in a mean-field manner by

$$\begin{aligned} F =& \mathrm{e}\Psi(N_+ - N_-) + B_+N_+^2 + B_-N_-^2 + CN_+N_- \\ & - k_\mathrm{B}T\ln\frac{N!}{(N-N_+-N_-)!N_+!N_-!}. \end{aligned} \tag{3.7}$$

Here, the first term is for the electrostatic potential interaction. The second, third, and fourth terms take into account for specific interactions between cations and anions.

In addition to the free energy equation, the electrostatic potential and the ion distributions are related via the Poisson equation,

$$\epsilon^*\frac{d^2\Psi}{dz^2} = 4\pi\mathrm{e}[c_- - c_+], \tag{3.8}$$

where $c_- = N_-/N$ and $c_+ = N_+/N$ are concentrations of anions and cations, respectively. If we approximate the eqn. 3.7 by assuming $B_+ = B_- = C = 0$, we can obtain following ion distributions as a function of Ψ by minimizing the free energy with respect to N_+ and N_-.

$$\begin{aligned} c_+ &= c_0\frac{\exp\left(-\frac{\mathrm{e}\Psi}{k_\mathrm{B}T}\right)}{1-\gamma+\gamma\cosh\left(\frac{\mathrm{e}\Psi}{k_\mathrm{B}T}\right)}, \\ c_- &= c_0\frac{\exp\left(\frac{\mathrm{e}\Psi}{k_\mathrm{B}T}\right)}{1-\gamma+\gamma\cosh\left(\frac{\mathrm{e}\Psi}{k_\mathrm{B}T}\right)}. \end{aligned} \tag{3.9}$$

The ion distributions can be controlled by a single parameter $\gamma = \overline{N}/N = 2c_0/c_\mathrm{max}$.

Combination of eqn. 3.8 and 3.9 gives the following Poisson-Fermi equation

$$\frac{d^2\Psi}{dz^2} = \frac{8\pi\mathrm{e}c_0}{\epsilon^*}\frac{\sinh\left(\frac{\mathrm{e}\Psi}{k_\mathrm{B}T}\right)}{1+2\gamma\sinh^2\left(\frac{\mathrm{e}\Psi}{2k_\mathrm{B}T}\right)}. \tag{3.10}$$

If we integrate this equation with the boundary conditions (i) the Gaussian law at the electrode/electrolyte interface $-\epsilon^*(d\Psi/dz)|_{z=0} = 4\pi\sigma$, where σ is the surface charge density, and (ii) the electric field in the bulk $(d\Psi/dz)|_{z\to\infty} = 0$, we can obtain the potential profile $\Psi(z)$. From $\Psi(z)$, the capacitance is obtained via $C = (d\sigma/dV)$, where $V = \Psi(0)$ is the potential drop across the EDL. The capacitance can be expressed as a function of dimensionless potential drop $u = \mathrm{e}V/k_\mathrm{B}T$,

$$C = C_\mathrm{D}\cosh\Big(\frac{u}{2}\Big)\frac{1}{1+2\gamma\sinh^2\big(\frac{u}{2}\big)}\sqrt{\frac{2\gamma\sinh^2\big(\frac{u}{2}\big)}{\ln\Big[1+2\gamma\sinh^2\big(\frac{u}{2}\big)\Big]}}, \qquad C_D = \frac{\epsilon^*}{4\pi\lambda_\mathrm{D}}, \qquad \lambda_\mathrm{D} = \sqrt{\frac{\epsilon^* k_\mathrm{B}T}{8\pi\mathrm{e}^2 c_0}}. \tag{3.11}$$

The resulting capacitance shows bell-shape to camel-shape transition with increasing ion density γ. This transition can be understood as *overscreening* and *crowding* effect of ions.

3.2.3 Constant potential simulation

In the present study, a constant potential method (CPM) in which the electrode atomic charge fluctuates with respect to the electrostatic potential is used to describe the electrode state.[85,86] In the CPM, the charge of the electrode atom $Q_i(\mathbf{r})$ at position R_i is expressed as a Gaussian function which is allowed to flucutuate, while the charge of electrolyte atom $q_j(\mathbf{r})$ at r_j is expressed as a delta function, as following equation,

$$\begin{aligned} Q_i(\mathbf{r}) &= Q_i\Big(\frac{\eta^2}{\pi}\Big)^{3/2}\mathrm{e}^{-\eta^2(\mathbf{r}-\mathbf{R}_i)^2}, \\ q_j(\mathbf{r}) &= q_j\delta(\mathbf{r}-\mathbf{r}_j). \end{aligned} \tag{3.12}$$

The electric potential Ψ_l on each electrode atom l is constrained to be an external potential V at every time step. This constraint leads to the following equation for the electrode atom charge Q_l.

$$\begin{aligned} V = \Psi_l &= \frac{\partial U}{\partial Q_l}, \\ \Psi_l &= \Psi_l^{\text{kspace}} + \Psi_l^{\text{real}} + \Psi_l^{\text{self}} + \Psi_l^{\text{slab}}. \end{aligned} \tag{3.13}$$

Here, Ψ_l^{kspace}, and Ψ_l^{real} are respectively k-space and real-space contribution in Ewald expression as following equations.

$$\begin{aligned} \Psi_l^{\text{kspace}} &= \frac{1}{V} \sum_{\mathbf{k}>0} \Gamma(\kappa)[\mathrm{e}^{-i\mathbf{k}\cdot\mathbf{R}_l} S(\mathbf{k}) + \mathrm{e}^{i\mathbf{k}\cdot\mathbf{R}_l} S(-\mathbf{k})], \\ \Gamma(\kappa) &= \frac{4\pi \mathrm{e}^{-\kappa^2/4\alpha^2}}{\kappa^2}, \\ S(\mathbf{k}) &= \sum_{i=1}^{n} Q_i \mathrm{e}^{i\mathbf{k}\cdot\mathbf{R}_i} + \sum_{j=1}^{m} q_j \mathrm{e}^{i\mathbf{k}\cdot\mathbf{r}_j}. \end{aligned} \tag{3.14}$$

$$\begin{aligned} \Psi_l^{\text{real}} = &\sum_{i=1}^{n'} q_i \frac{\operatorname{erfc}(\alpha r_{li}) - \operatorname{erfc}(\frac{\eta}{\sqrt{2}} r_{li})}{r_{li}} \\ &+ \sum_{j=1}^{m} q_j \frac{\operatorname{erfc}(\alpha r_{lj}) - \operatorname{erfc}(\eta r_{lj})}{r_{lj}}, \end{aligned} \tag{3.15}$$

where n' is denotes the number of electrode atom in which $i = l$ term is excluded, m is the number of electrolyte atom.

Ψ_l^{self} and Ψ_l^{slab} are self correction and slab-geometry correction terms, respectively.

$$\Psi_l^{\text{self}} = \frac{\sqrt{2}\eta - 2\alpha}{\sqrt{\pi}} Q_l, \tag{3.16}$$

$$\Psi_l^{\text{slab}} = \frac{4\pi Z_l}{V}\Big(\sum_{i=1}^{n} Q_i Z_i + \sum_{j=1}^{m} q_j z_j\Big), \tag{3.17}$$

where Z_i is the z component electrode atom position and z_j is the corresponding quantity for an electrolyte atom.

The potential expression can be rewritten as following linear equation of Q_i and q_j.

$$\begin{aligned} \Psi_l &= \sum_{i}^{n} a_{li} Q_i + \sum_{j}^{m} b_{lj} q_j \\ \sum_{i}^{n} a_{li} Q_i &= V - \sum_{j}^{m} b_{lj} q_j \\ \mathbf{AQ} &= \mathbf{V} - \mathbf{B} \end{aligned} \tag{3.18}$$

From solving this linear equation, the explicit charge for electrode atoms can be determined at every time step.

3.3 Simulation Methods and Models

3.3.1 System descriptions

In our simulation system, two parallel graphene walls were used as the electrodes, and $[EMIM]^+[SCN]^-$ ionic liquid confined between them was used as an electrolyte.(Figure 3.2) A total of 256 ion pairs are used as electrolyte molecules, and each electrode consists of 448 carbon atoms with the dimension of 33.96×34.31 Å^2. The distance between the two electrodes is fixed as 60 Å, which is wide enough that the middle part of the system forms a bulk phase. The system size was determined via NPT MD simulation of the pure $[EMIM]^+[SCN]^-$ liquids. Ions were modeled with flexible OPLS all-atom force fields. Parameters of the $[EMIM]^+$ cation were taken from the study on the imidazolium-based ionic liquids,[87,88] and the $[SCN]^-$ anion parameters were taken from a previous study of cyano-anion ionic liquids.[89] Exact parameters are compiled in the supporting information of the references reported by Canongia Lopes et al.[87] and Dhungana et al.[89]. Graphene atoms were described as fixed Lennard-Jones particles with a diameter of $\sigma_{LJ} = 3.4$ Å and a depth of the potential well of $\epsilon_{LJ} = 0.086$ kcal/mole.[90] Force-field parameters between different atomic species were evaluated from the Lorentz-Berthelot rules.

3.3.2 Simulation methods

All our MD simulations were performed using LAMMPS program.[91] The motion of particles were integrated using the velocity Verlet algorithm with 1 fs timestep. The cutoff distances for non-bonded interactions were set to 1.4 nm. Systems were equilibrated for longer than 10 ns using simulated

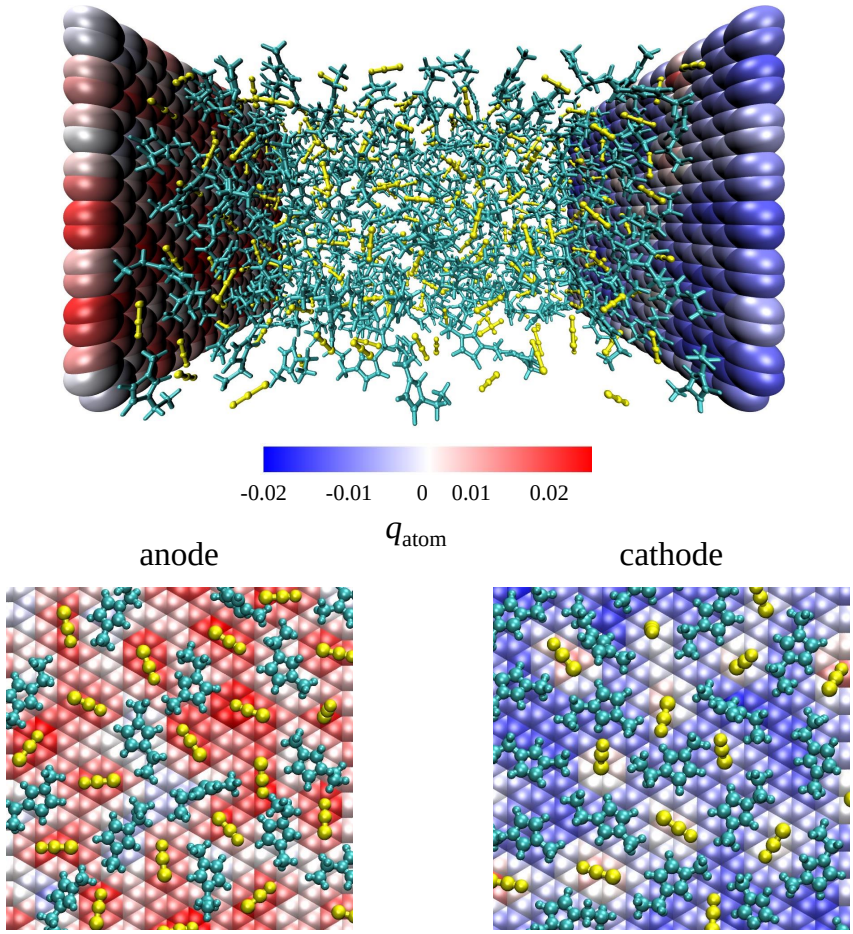

Figure 3.2: representative snapshots of our simulation at $\Delta\Psi = 2$ V. The charge of each electrode atom is indicated by its color, which is referred to color scale bar (unit e). Here, the left electrode is the anode, and the right one is the cathode. Between these electrodes, pure $[\mathrm{EMIM}]^+[\mathrm{SCN}]^-$ ions are filled as an electrolyte. $[\mathrm{EMIM}]^+$ and $[\mathrm{SCN}]^-$ ions are depicted as cyan and yellow moleuclar ions, respectively.

annealing from 800 K to 350 K, and production runs were conducted at 350 K. The temperature was controlled using Nosé-Hoover thermostat with a relaxation time of 100 fs during the NVT simulations. A constant potential method (CPM)[85] was applied to control the electrostatic potential between two electrodes. In this method, the charge of the electrode atoms are described as a Gaussian function, and they fluctuate during simulations to maintain the constant potential difference between the electrodes. The Gaussian function parameter for the graphene electrode is set to 19.79 nm^{-1}, which is the same as that of a three-layer graphite.[86] The charge of the electrolyte ion atoms are described as a fixed point charge. The CPM was conducted with the *conp* module implemented in the LAMMPS.[86] In this module, 3D-periodic Ewald summation with shape corrections[92] was applied to describe the slab geometry of the system, and the particle-particle particle-mesh (PPPM) method was used to evaluate the Coulombic interactions.[93]

3.4 Results and Discussions

3.4.1 Electrode charge fluctuation of the EDLC

We first validated our constant potential simulations on the graphene$-[EMIM]^+$ $[SCN]^-$ EDLC system. In our simulations, the electrostatic potential at the anode is higher than that of the cathode by $\Delta\Psi$. $\Delta\Psi$ is defined as $\Delta\Psi = \Psi_{\mathrm{anode}} - \Psi_{\mathrm{cathode}}$, where Ψ_{anode} and Ψ_{cathode} are the electrostatic potentials applied at the anode and the cathode, respectively. The anode and the cathode are charged with positive and negative potential values, respectively. The charge of each electrode atom is not fixed as a constant

value during simulation, but fluctuates depending on the local electrostatic environment and the potential bias applied in the system. As shown in Figure 3.2, both $[EMIM]^+$ and $[SCN]^-$ ions can be adjacent to the anode and cathode surfaces depending on the local environment, and the local charge induced on the electrode turns out to be highly correlated with the adjacent interfacial ions. The correlation can be analyzed by the distribution of individual charges of the electrode atoms.

Figure 3.3 shows the probability distribution of atomic charges in each electrode, $p(q_{\mathrm{atom}})$, under various $\Delta\Psi$ conditions. When $\Delta\Psi = 0$ V is applied, $p(q_{\mathrm{atom}})$ of two electrodes are in coincidence. However, when finite $\Delta\Psi$ is applied, the anode and the cathode are charged with opposite values, and the probability distribution for each electrode develops different characteristic behaviors. This asymmetry indicates that not only the electrodes have opposite charge values but also the environment around the two electrodes become completely different. It should be noted that the the probability distribution exhibits a non-Gaussian behavior at all potential conditions, even at $\Delta\Psi = 0$ V. For the organic electrolyte/salt-based EDLC, a non-Gaussian distribution has been observed only under high potential conditions.[86] The non-Gaussian nature in the ionic liquid EDLC is due to the high ionic density near the electrode surface and the asymmetric shape and charge distribution of the molecular ions. In addition, even when $\Delta\Psi$ is as large as up to 3 V, there always exists an atom with an opposite charge to the electrode charge due to the broad distribution of $p(q_{\mathrm{atom}})$. Overall, it is clear that the fluctuation of the electrode charge is critical in understanding the structure of the ionic liquid EDLC, so it is necessary to utilize the CPM in studying dynamical behavior of the EDLC of our system.

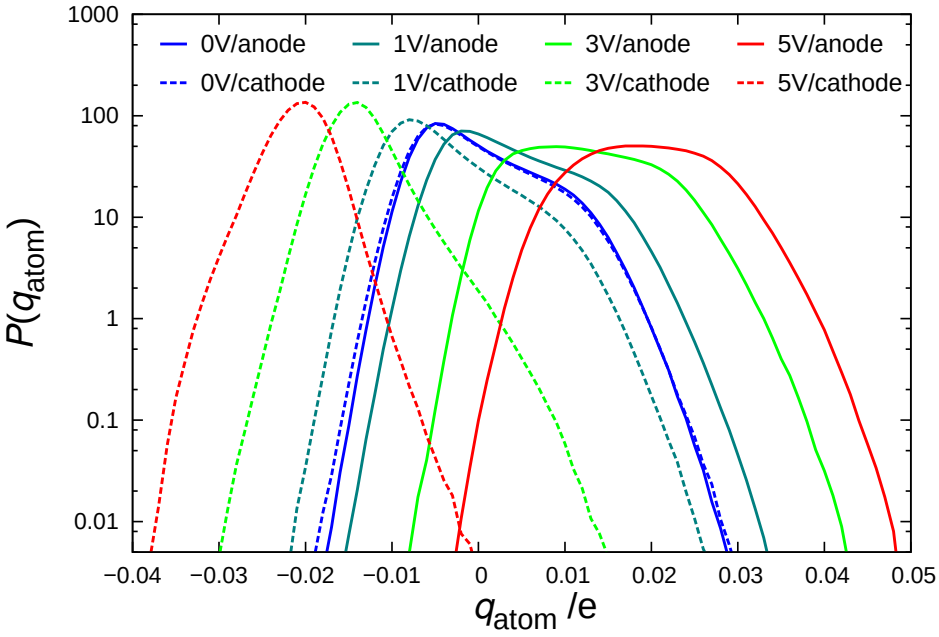

Figure 3.3: Distribution of electrode atom charges at the various electrostatic potential difference between the anode and the cathode, $\Delta\Psi$. The legend key is expressed as the form of "$\Delta\Psi$/electrode". Solid and dashed lines denote the distributions for the anode and the cathode, respectively.

3.4.2 Ionic layer structures in the EDLC

We investigated the ionic layer structure near the graphene electrodes via number density and charge density. Number density distribution $n_\alpha(z)$ of the specific ion α is defined as the integration of the center of mass distribution of ions $n_\alpha(x'.y', z)$, expressed as following equation,

$$n_\alpha(z) = A_0^{-1} \int_{-x_0}^{x_0} \int_{-y_0}^{y_0} dx'dy' n_\alpha(x', y', z). \tag{3.19}$$

Here, A_0 is the electrode surface area. Similar to the number density $n_\alpha(z)$, the charge density distribution $\rho_\alpha(z)$ is defined by the following equation,

$$\rho_\alpha(z) = A_0^{-1} \int_{-x_0}^{x_0} \int_{-y_0}^{y_0} dx'dy' \rho_\alpha(x', y', z), \tag{3.20}$$

where $\rho_\alpha(x', y', z)$ is the local atomic charge density of the ion α.

Figure 3.4 shows $n_\alpha(z)$ and $\rho_\alpha(z)$ in various $\Delta\Psi$ conditions. The anode and the cathode are located at $z = -30$ Å and $z = 30$ Å, respectively. The ions form the first ionic layer at 3.5 Å away from the electrode, which is the closest distance to the graphene surface due to the size of the particles. After the first ionic layer, the oscillating ion density along the z direction reflects the formation of additional ionic layers. This oscillating layer structure is a common feature in the ionic liquid EDLC.[41,94–96] When there is no potential difference between the electrodes, the maximum density positions of $[EMIM]^+$ and $[SCN]^-$ overlap with each other. This is because the local electroneutrality should be satisfied and the layer thicknesses of the two ions are similar to each other. However, when the electrodes are charged due to the finite potential difference, the first ionic layer is filled with counter-ions, while co-ions are expelled from the electrode. If a potential difference greater

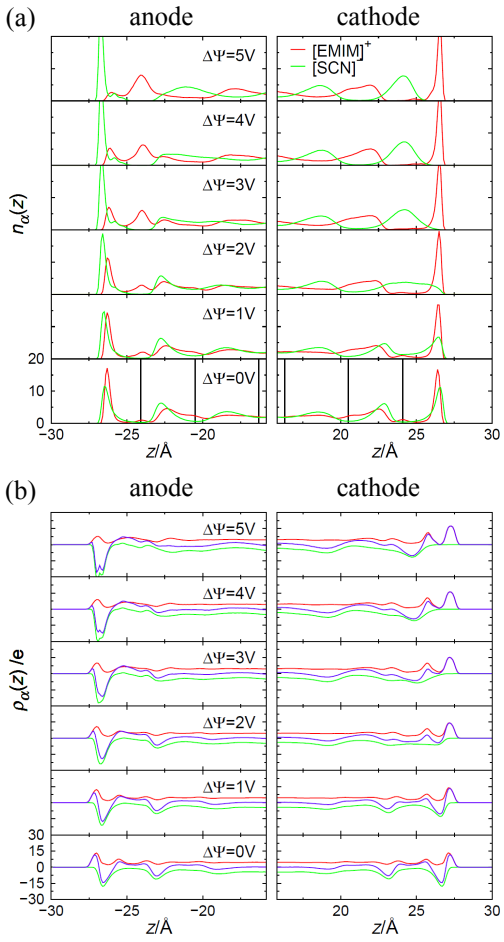

Figure 3.4: (a) $n_\alpha(z)$ and (b) $\rho_\alpha(z)$ of $[\mathrm{EMIM}]^+$ and $[\mathrm{SCN}]^-$ ions. The anode and the cathode are located at $z = -30$ Å and $z = 30$ Å, respectively. The values for cations and anions are represented as red and green, respectively. Black vertical lines denote the minimum positions of $n_{[\mathrm{SCN}]^-}(z)$ in $\Delta\Psi = 0$ V condition. Purple lines in the charge density $\rho_\alpha(z)$ denote the total charge density, which is defined as $\rho_{\mathrm{total}}(z) \equiv \rho_{[\mathrm{EMIM}]^+}(z) + \rho_{[\mathrm{SCN}]^-}(z)$.

than 3 V is applied, the alternating layers of the counter-ions and co-ions are formed. Particularly, the ionic layer structure changes abruptly under $\Delta\Psi = 2$ V condition: the first and the second $[SCN]^-$ ion layers near the cathode merge into their intermediate position.

Charge densities of $[EMIM]^+$ and $[SCN]^-$ ions also show oscillations with respect to the z direction near the electrode surface. When we compare $\rho_\alpha(z)$ and $n_\alpha(z)$, the oscillatory behavior of the charge density almost disappears within 10 Å from the electrode, while that of the number density persists beyond that distance. This observation indicates that molecular ions efficiently rearrange themselves by maximizing the Coulomb interaction with other particles in the vicinity.[48,73,97] Interestingly, all the charge densities from the electrodes initially show positive peaks even near the anode in $\Delta\Psi = 4$ V condition. Under the potential condition we consider, $[SCN]^-$ ions cannot fully replace the $[EMIM]^+$ ions in the first layer due to a strong $\pi - \pi$ stacking interaction between the cations and graphene electrodes. It is worth noting that the ionic layer structures of Figure 3.4 are consistent with those from the work done under the constant charge condition,[58] and the direct comparison between the two is depicted in Figure 3.5. A good agreement arises because the fluctuation of the electrode charge is averaged out for the static thermodynamical properties in equilibrium. However, it does not mean that the electrode charge fluctuation is unimportant in the dynamical properties of the EDLC. To the contrary, the opposite is the case as will be shown later.

So far, we have studied the structure of the ionic layer according to the distance from the electrode surface. However, in order to better understand the ionic layer structure, not only the distance from the electrode but also

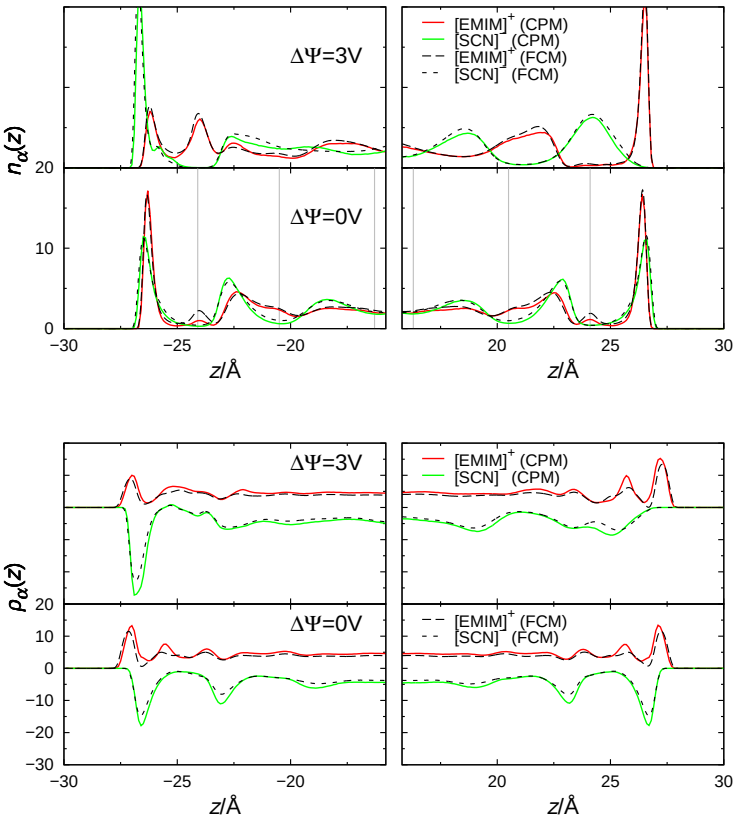

Figure 3.5: $n_\alpha(z)$ and $\rho_\alpha(z)$ calculated in a CPM and a FCM. Color solid lines and black dashed lines denote the data from CPM and FCM, respectively. Applied potential differences between the electrode in CPM are $\Delta\Psi = 0$ V and $\Delta\Psi = 3$ V, and the corresponding charge densities of the electrodes in FCM are 0 e/Å^2 and ± 0.0043 e/Å^2.

the orientation of the ions must be considered simultaneously. To describe the orientation of each ion, the angles $\theta^{\pm}$ are defined as follows. For $[EMIM]^+$ ions, θ^+ is defined as an angle between an electrode normal vector and an $[EMIM]^+$ ring normal vector, while θ^- of $[SCN]^-$ ions is defined as an angle between an electrode normal vector and a vector from a nitrogen atom to a sulfur atom in $[SCN]^-$ ion. For clarity, the graphical description of $\theta^{\pm}$ is presented in the Figure 3.6. According to these definitions, $\cos\theta^+$ and $\cos\theta^-$ are equal to 1 and 0, respectively, when the corresponding ions are parallel to the electrode.

Figure 3.6 shows the probability distribution of ions with respect to $\cos\theta^{\pm}$ and Δz, the distance from the electrode. When no potential bias is applied, both $[EMIM]^+$ and $[SCN]^-$ ions adjacent to the graphene electrodes maintain a parallel arrangement with respect to the electrodes. The parallel arrangement of the $[EMIM]^+$ ions is due to that the $[EMIM]^+$ ions form a strong $\pi - \pi$ stacking interaction with electrodes. The $[SCN]^-$ ions also maintain a parallel arrangement with respect to the electrodes to maximize the Coulombic interaction with the parallely aligned $[EMIM]^+$ ions. Since the thicknesses of the two ions forming the ionic layer are equal to that of a single carbon atom, the neighboring ionic layers are arranged similar to the first ionic layer. As a result, the orientation of ions is maintained as parallel until the third layer, indicating that the ionic layer is not a localized structure only next to the electrode.

When $\Delta\Psi = 3$ V is applied, ionic layers near each electrode change in distinct manners. In the vicinity of the anode, a portion of $[EMIM]^+$ ions forming $\pi - \pi$ stacking with the electrode rotate in the vertical direction and desorb from the electrode. As this pre-emptied space becomes filled

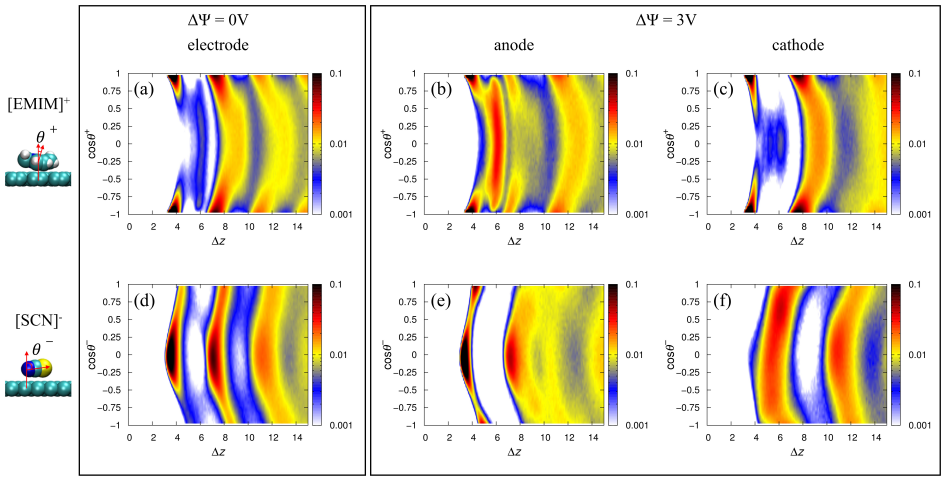

Figure 3.6: The contour map of the ionic layer structures. Δz denotes the distance of the ion from the electrode, and $\cos\theta^{\pm}$ denotes the orientation of specific ions. The graphical description of angles $\theta^{\pm}$ are presented at the left panel. The probability density increases in the order of white-blue-yellow-red-black. (a), (d) The contour map of $[EMIM]^+$ and $[SCN]^-$ ions when zero electrode potential is applied. (b), (c) The contour map of $[EMIM]^+$ ions near the anode and cathode when electrode potential $\Delta\Psi = 3$ V is applied. (e), (f) The contour map of $[SCN]^-$ ions near the anode and cathode when electrode potential $\Delta\Psi = 3$ V is applied.

with $[SCN]^-$ ions coming from the second layer, the density of $[SCN]^-$ ions in the first ionic layer increases. Looking at the ionic layer near the cathode, $[SCN]^-$ ions parallel to the electrode rotate and desorb from the electrode, and vertically aligned $[EMIM]^+$ ions form $\pi-\pi$ stacking structure to the electrode. That is, the rearrangement of the ionic layer due to the polarization of the electrode is accompanied by rotational movements of the ions near the electrode. During the rearrangement of ionic liquids, not only the first and second ionic layers but also further ionic layers undergo significant structural changes.

As discussed in the behavior of the charge density, $\rho_\alpha(z)$, $[EMIM]^+$ ions, which is the co-ion of the anode, form a $\pi-\pi$ stacking structure with the anode, while $[SCN]^-$ ions are completely expelled from the cathode. This finding indicates that the structural rearrangement of bulky and heavy $[EMIM]^+$ ions is much more difficult than $[SCN]^-$ ions. Therefore, it is further expected that the ionic layer change and corresponding energy stored in the EDLC are dominated by the rearrangement of $[SCN]^-$ ions.

3.4.3 Differential capacitance

Electrostatic potential profile of the EDLC along the z direction, $\Psi(z)$, can be calculated by integrating the Poisson equation of the charge density $\rho(z)$ as following,

$$\Psi(z) = -4\pi \int_{-\infty}^{z} (z - z')\rho(z')dz'. \tag{3.21}$$

The calculated $\Psi(z)$ in various $\Delta\Psi$ conditions are depicted in Figure 3.7. Similar to $n_\alpha(z)$ and $\rho_\alpha(z)$ in Figure 3.4, $\Psi(z)$ also shows an oscillatory behavior, indicating the existence of multiple ionic layers. The electrostatic

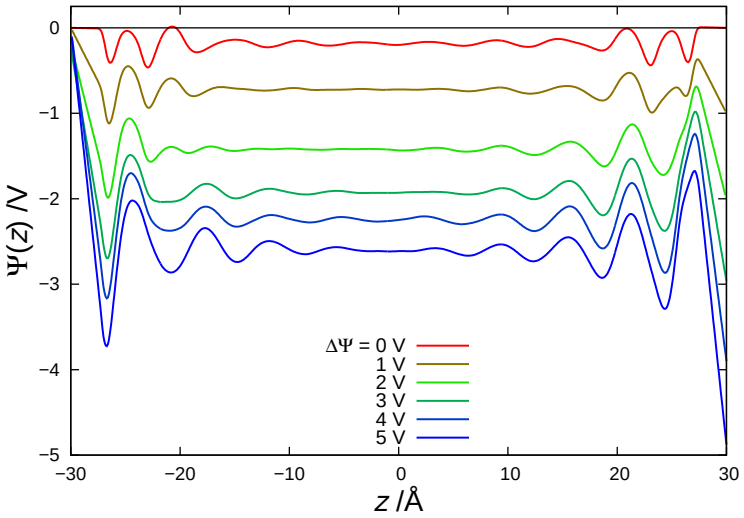

Figure 3.7: Electrostatic potential $\Psi(z)$ as a function of z. The anode and cathode are located at -30 Å and 30 Å, respectively.

potential profile becomes nearly constant in the bulk region after sharp decreases near the electrode. Thus, the entire EDLC can be described as a series connection of the anode and cathode half-cells. The corresponding potential drop of each half-cell is defined as following equation,

$$\begin{aligned} \Delta\Psi_{\text{half}}^{\text{anode}} &\equiv \Psi_{\text{anode}} - \Psi_{\text{bulk}}(z = 0 \text{ Å}), \\ \Delta\Psi_{\text{half}}^{\text{cathode}} &\equiv \Psi_{\text{cathode}} - \Psi_{\text{bulk}}(z = 0 \text{ Å}), \\ \Delta\Psi &= \Delta\Psi_{\text{half}}^{\text{anode}} - \Delta\Psi_{\text{half}}^{\text{cathode}}. \end{aligned} \tag{3.22}$$

The potential of zero charge (PZC) is defined as $\Delta\Psi_{\text{half}}$ in $\Delta\Psi = 0$ V condition. PZC is calculated as 0.20 V, and such a positive PZC indicates the larger affinity of the graphene electrode for $[\text{EMIM}]^+$ ions due to the

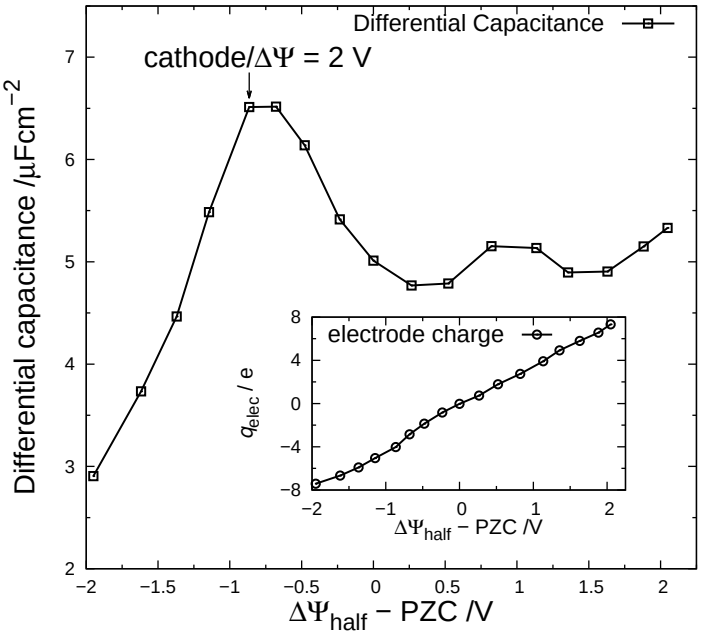

Figure 3.8: Differential capacitance of EDLC as a function of Ψ_{half}. (inset) Electrode charge as a function of Ψ_{half}.

$\pi - \pi$ interaction between them.

With the definition of the half-cell, the relation between $\Delta\Psi_{\mathrm{half}}$ and the corresponding electrode charge, q_{elec}, is depicted in the inset of Figure 3.8. q_{elec} increases almost linearly with $\Delta\Psi_{\mathrm{half}}$, and the derivative of q_{elec} with respect to $\Delta\Psi_{\mathrm{half}}$ is related to the area-specific differential capacitance (DC) as the following equation,

$$\mathrm{DC}(\Delta\Psi_{\mathrm{half}}) = \frac{\partial q_{\mathrm{elec}}}{A_0 \partial \Delta\Psi_{\mathrm{half}}}, \tag{3.23}$$

where A_0 is the area of the electrode. The differential capacitances were evaluated via the analytical derivative of the parabola fit of q_{elec} vs. $\Delta\Psi_{\mathrm{half}}$ plot.[57] Corresponding DC of the $[\mathrm{EMIM}]^+[\mathrm{SCN}]^-$−EDLC shows a camel-like distribution, exhibiting a minimum near the PZC and maximum at higher potential. The maximum of the DC occurs at $\Delta\Psi_{\mathrm{half}} = \mathrm{PZC} - 0.865$ V, which corresponds to the cathode at $\Delta\Psi = 2$ V condition. Interestingly, the first layer of $[\mathrm{SCN}]^-$ ion near the cathode is also entirely expelled from the electrode at the $\Delta\Psi = 2$ V condition, as depicted in the Figure 3.4. This may be called a *vacating* effect, in which the desorption of co-ions from the electrode mainly contributes to the capacitance of the EDLC. The vacating effect has also been observed in other EDLC systems based on graphene oxide.[39,98] The most important factor for inducing the vacating effect is the high ion density near the electrode. Therefore, the vacating effect is expected to be common in EDLCs with ionic liquids electrolytes and planar electrodes, and indicates that the performance of the EDLC is closely related to the rearrangement of the ionic layer.

3.4.4 Charging dynamics

In order to investigate the charging dynamics of the EDLC, we conduct the non-equilibrium MD simulation by applying the constant potential differences $\Delta\Psi$ between equilibrium electrodes of $\Delta\Psi = 0$ V. Firstly, the influence of the applied potential difference $\Delta\Psi$ on the charging dynamics is examined. For each condition, at least five independent trajectories are averaged out in order to reduce the statistical noise. Fig. 3.10 (a) shows the evolution of the charge density of electrodes $\sigma(= q_{\mathrm{elec}}/A_0)$ during charging. Under all conditions, most of the charging process is finished within a few hundred

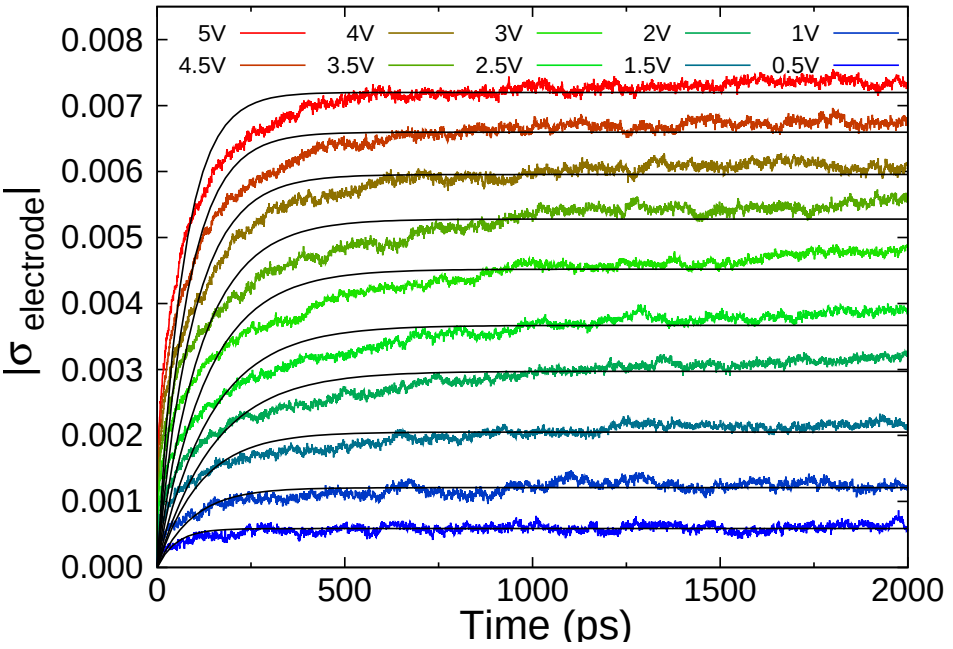

Figure 3.9: Evolution of the electrode charge density during charging. Color lines are simulation data, and black solid lines are the corresponding fitting curves with the single exponential function.

picoseconds, followed by an additional slow charging dynamics.

To quantitatively analyze the charging dynamics, we tried to fit the evolution of electrode charge density by a single exponential function without any success. This deficiency occurs because the capacitance of the supercapacitor is not constant during charging, and charging dynamics is dependent on the heterogeneous dynamics of the ionic liquids.[99–101] Thus, two kinds of relaxation functions which have been used for the dynamically heteroge-

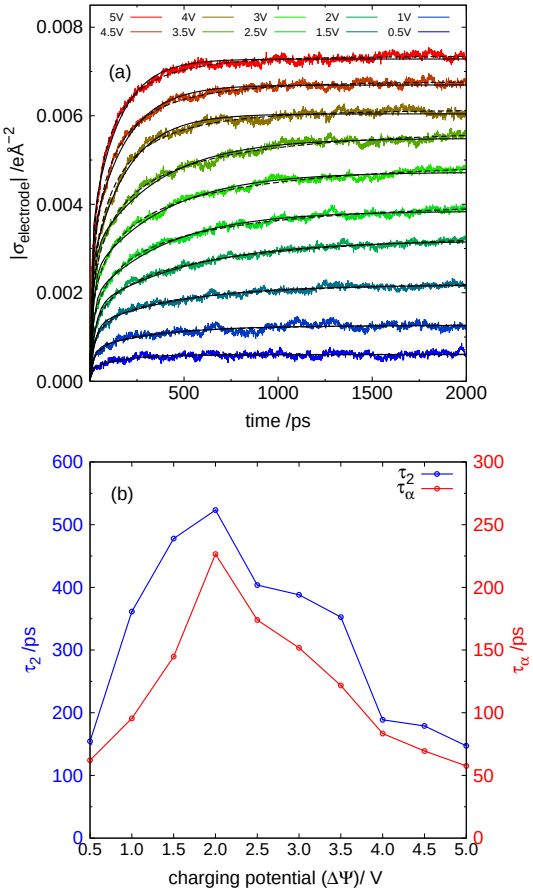

Figure 3.10: (a) The charge of the electrode relaxations as a function of time when finite potentials are applied to the equilibrium states of $\Delta\Psi = 0$ V. Black solid and dashed lines are fitted curves with bi-exponential and stretched exponential functions, respectively. (b) The charging time of the EDLC as a function of $\Delta\Psi$. Blue and red lines respectively denote the τ_2 from bi-exponential fitting and τ_α from stretched exponential fitting.

Table 3.1: Relaxation times and stretching exponents of the charging dynamics of the EDLC

$\Delta\Psi$	τ_1/ps	τ_2/ps	τ_α/ps	β
0.5	3.39	154.46	62.10	0.489
1.0	20.88	361.41	95.52	0.435
1.5	24.38	477.85	144.79	0.397
2.0	26.27	523.29	226.53	0.403
2.5	17.43	403.67	173.95	0.429
3.0	16.63	388.14	151.25	0.419
3.5	16.95	352.60	121.72	0.437
4.0	6.98	188.79	83.41	0.533
4.5	9.02	178.93	69.47	0.522
5.0	8.36	147.22	57.57	0.532

neous system are applied, (1) bi-exponential and (2) stretched exponential functions. They are given by the following equations,

$$\sigma(t) = \sigma_{t=\infty}[1 - c\exp(-t/\tau_1) - (1-c)\exp(-t/\tau_2)], \tag{3.24}$$

where $c, \tau_1, \tau_2, \sigma_{t=\infty}$ are fitting parameters, and

$$\sigma(t) = \sigma_{t=\infty}[1 - \exp(-(t/\tau_\alpha)^\beta)], \tag{3.25}$$

where $\tau_\alpha, \beta, \sigma_{t=\infty}$ are fitting parameters. Both fitting functions show good agreements with the simulation results, as shown in Figure 3.10. The relaxation times $\tau_1, \tau_2, \tau_\alpha$ and stretching exponent β are tabulated in TABLE 3.1.

In most cases, τ_2 is about 20 times of τ_1, which means that the motions with large differences in time scale coexist in the system. In addition, β has a value of 0.40 to 0.54, indicating that the charging dynamics is far from a single exponential relaxation process. These properties, as expected, indicate that the charging dynamics of the EDLC follows heterogeneous dynamics. In addition, the relaxation time exhibits an interesting non-monotonous behavior which shows a maximum value when the applied potential $\Delta\Psi$ is 2 V. As discussed above for the number density of ions $n_\alpha(z)$, the greatest transition in the ionic layer structure occurs at $\Delta\Psi \sim 2$ V condition as $[SCN]^-$ ions in the first layer adjacent to the cathode are expelled from the surface. It is not a coincidence that the ionic layer changes abruptly under the potential condition and shows the slowest charging dynamics. The charge of the electrode is proportional to the applied potential, while the layer structure changes abruptly under $\Delta\Psi \sim 2$ V condition and is almost constant thereafter. This observation means that the charging dynamics of the EDLC is highly correlated with the rearrangement of the ionic layer structure. From this correlation between the charging dynamics and the ionic layer structure, we can determine the conditions under which the ionic layer undergoes an abrupt structural rearrangement in the EDLC by measuring the charging time of the EDLC.

The evolution of the ionic layer structure during the charging of the EDLC is depicted in Figure 3.11. The figure represents the $n_\alpha(\Delta z)$ as a function of time when constant $\Delta\Psi = 3$ V is applied to the unbiased equilibrium state. The ionic layers continuously change from layer structure of 0 V to that at the 3 V. In all cases, except for $[SCN]^-$ ions near the cathode, the first ionic layers located at $\Delta z = 3.5$ Å are maintained during charging.

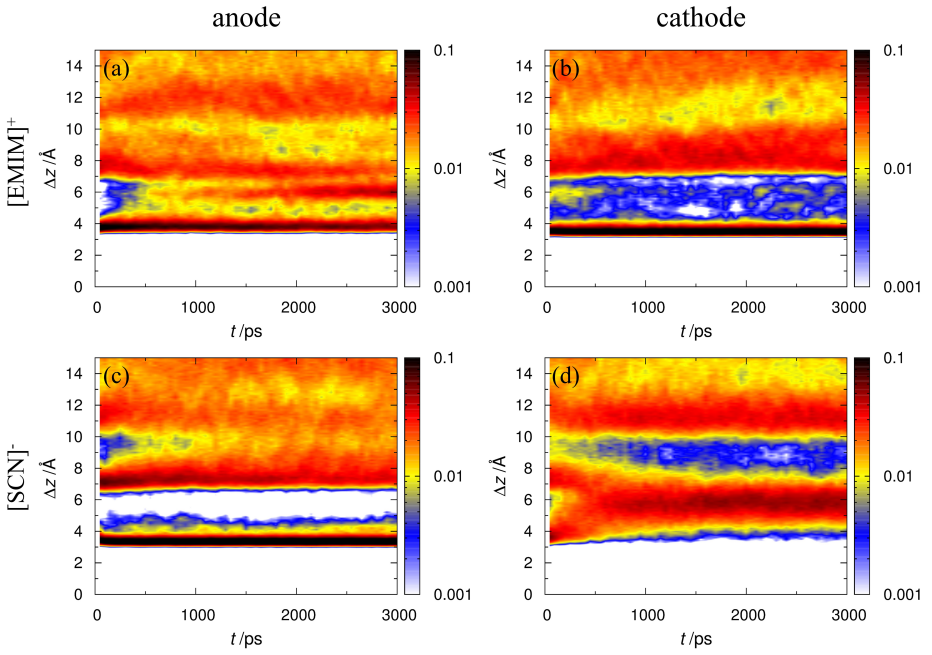

Figure 3.11: Evolution of the number density of ions, $n_\alpha(\Delta z)$ as a function of time when $\Delta\Psi = 3$ V is applied. The probability density increases in the order of white-blue-yellow-red-black. Each panel represents the density of $[EMIM]^+$ ions near (a) the anode and (b) the cathode, and $[SCN]^-$ ions near (c) the anode and (d) the cathode.

Only $[SCN]^-$ ions adjacent to the cathode are completely expelled from the electrode. The ionic layer structure of the counter-ions is almost constant during the 3 ns simulations, but the co-ion layer structure evidently changes during the charging, especially in $[SCN]^-$ ions near the cathode.

As mentioned before, the relaxation of the ionic layer structure cannot be described by a single time scale. The density of the interfacial ions relaxes within a very short time, but the structure of the overall ionic layer relaxes for more than 1 ns, which is consistent with the fact that the charge of the electrode is charged on multiple time scales as depicted in Figure 3.10. The multiple time scale motions in charging of the EDLC was also reported in the time-resolved X-ray experiment.[102] In their experimental study, the authors found that the time scale of the reorientation of interfacial ions was one order of magnitude larger than the time scale of the diffusion-limited ion transport, which is consistent with our findings. From the evolution of the ionic layer structure, it is suggested that the charging process of the EDLC occurs via multiple time scales. When the electrode is charged, the interfacial ions respond sensitively to the electrode charge through a diffusion within the existing ionic layer. However, if the increased electrode charge cannot be screened by the diffusive motion of ions within the first ionic layer, the electrode charge is screened by rearranging the overall ionic layer structure. The ionic layer rearrangement proceeds over a larger time scale than the diffusive motion of ions within the layer, and such a multi-stepwise motion of ions results in a heterogeneous charging dynamics.

So far, it has been confirmed that the charging of the EDLC is greatly influenced by the ionic layer structure transitions. To analyze the correlation between electrode charge and ionic layer structure quantitatively, we

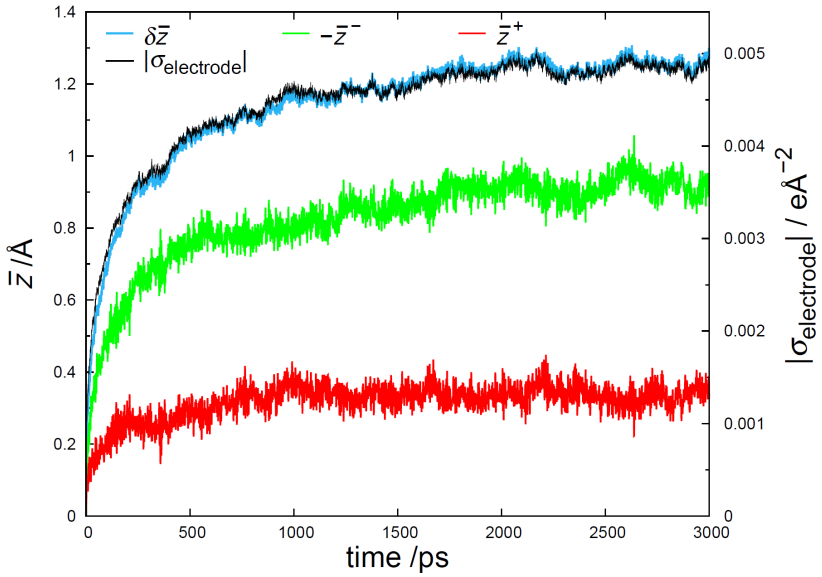

Figure 3.12: Evolution of the center of mass of ions and charge of the anode when electrode is charged with $\Delta\Psi = 3$ V. Blue, gren, and red lines represent $\delta\overline{z}$, $-\overline{z}^{-}$, and $\overline{z}^{+}$, respectively. The black line represents the electrode charge density, $|\sigma_{\text{electrode}}|$.

calculate the average perpendicular displacement of α ions with respect to the electrode, $\overline{z}^{\alpha}$, defined by

$$\begin{aligned} \overline{z}^{\alpha}(\Delta t) &= \frac{1}{N^{\alpha}} \sum_{i=1}^{N^{\alpha}} [z_i^{\alpha}(t = \Delta t) - z_i^{\alpha}(t = 0)], \\ \delta\overline{z} &= \overline{z}^{+} - \overline{z}^{-}, \end{aligned} \tag{3.26}$$

where N^{α} is the number of α ions, and $z_i^{\alpha}(t)$ is the z component of the ith α ion position at time t. Figure 3.12 shows that the evolution of the electrode

charge is consistent with $\delta\overline{z}$, the difference between $\overline{z}^{+}$ and $\overline{z}^{-}$. This is because that the energy stored in the EDLC during the charging induces the rearrangement of the electrolyte, and the amount can be quantified with $\delta\overline{z}$. $\delta\overline{z}$ is a scalar quantity which can be simply calculated by averaging the perpendicular displacement of ions without considering a complex ionic layer structure. In other words, we can calculate how much each ionic species contributes to the stored charge in EDLC by calculating their perpendicular displacements. As described in Figure 3.12, about 75% of charge stored on the electrode is induced by the rearrangement of $[SCN]^{-}$ ions, which is consistent with the observation that the differential capacitance of the EDLC is dominated by desorption of the anion.

Based on the fact that the electrode charge is consistent with the perpendicular displacement of ions, we can calculate how each ionic layer contributes to the electrode charge. Ions are distinguished according to the distance from the electrode at the beginning of the charging simulations. As mentioned for $n_{\alpha}(z)$, at $\Delta\Psi = 0$ V, the ionic layers of $[EMIM]^{+}$ and $[SCN]^{-}$ ions are positioned at the same location because of their parallel alignment to the electrode. Thus, the three ionic layers from the electrode surface are classified through the boundary at which $n_{[SCN]^{-}}(z)$ is minimum. As depicted by the black vertical lines in Figure 3.4, the ions located at $\Delta z = 0 \sim 5.9,\ 5.9 \sim 9.5,\ 9.5 \sim 13.7$ Å are defined as the 1st, 2nd and 3rd ionic layers, respectively. The ions 13.7 Å or more away from the electrode are defined as bulk ions. It has been checked that our discussion does not alter qualitatively even if the boundary values change slightly.

The total perpendicular displacement of the lth ionic layer of α ion

species, $\overline{Z}_l^{\alpha}$, is defined as

$$\overline{Z}_l^{\alpha}(\Delta t) = \sum_{i=1}^{N_l^{\alpha}} [z_i^{\alpha}(t = \Delta t) - z_i^{\alpha}(t = 0)], \quad \text{where } \{i | z_i^{\alpha}(t = 0) \in l\text{th layer}\}. \tag{3.27}$$

Here, N_l^{α} is the number of α ions in the lth layer at time $t = 0$. Therefore, $\overline{Z}_l^{\alpha}$ represents the sum of the perpendicular displacement of α ions belonging to the lth layer at time $t = 0$. In addition, $\delta\overline{Z}_l$ is defined as following equation.

$$\delta\overline{Z}_l = \overline{Z}_l^{+} - \overline{Z}_l^{-} \tag{3.28}$$

Similar to $\delta\overline{z}$, $\delta\overline{Z}_l$ can be interpreted as a contribution of the lth ionic layer to the charge stored in the EDLC. The time evolution of $\delta\overline{Z}_l$ when EDLC is charging under $\Delta\Psi = 3$ V condition is depicted in Fig. 3.13. Even though the applied potential is different, the evolution of the $\delta\overline{Z}_l$ is not significantly affected. In addition, the ionic displacement occurs not only in a particular layer but also in all ionic layers

The contribution of each layer to the electrode charge is compared through $\delta\overline{Z}_l$ at $\Delta t = 3$ ns, within which the charging process is complete. Figure 3.14 shows the corresponding contribution of all ionic layers and their constituent ions. The histogram summarizes our findings. (1) In the vicinity of the electrode, the contribution of the co-ion of the electrode is greater than that of the counter-ion. Due to the geometric interaction of the electrodes, the counter-ions in the first ionic layer can no longer get close to the electrodes, but the co-ions can easily fall into the bulk area. This vacating effect expected to be common in the EDLC consisting of ionic liquid electrolytes and planar electrodes. (2) The contribution of the bulk ions is

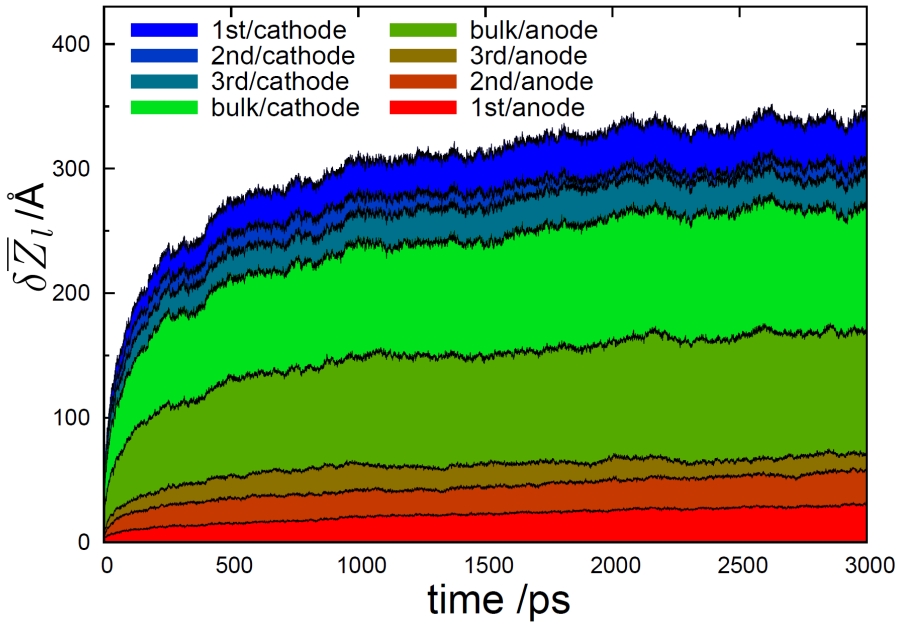

Figure 3.13: $\delta\overline{Z}_l(\Delta t)$ of each ionic layer when EDLC is charged with $\Delta\Psi =$ 3 V. $\delta\overline{Z}_l$ value of each layer is depicted as the colored area.

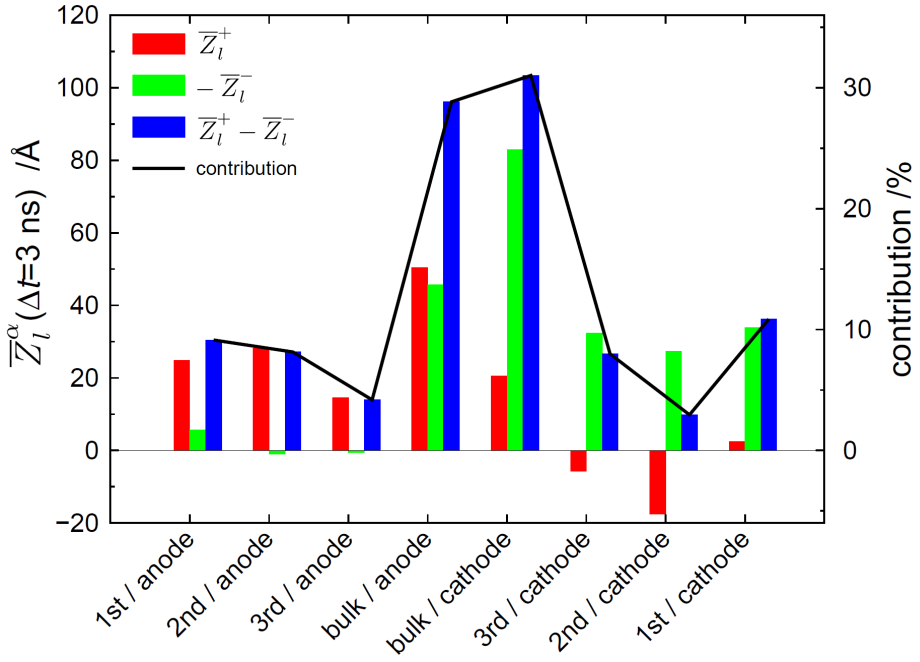

Figure 3.14: The histogram of the extensive displacement of the lth ionic layer at $\Delta t = 3$ ns. The blue bar denotes $\delta\overline{Z}_l(\Delta t = 3\text{ ns})$ of each layer, which can be interpreted as the electrode charge contribution of the corresponding layer, as depicted by the black line. Red and green bars represent $\overline{Z}_l^+(\Delta t = 3\text{ ns})$ and $-\overline{Z}_l^-(\Delta t = 3\text{ ns})$, respectively.

more than half of the entire system. The important role of bulk ions in the EDLC is in contrast to the conventional idea that the electric double layer within a subnanometer scale completely screens the electrode charges. The conventional electric double layer concept should be used with great caution in the ionic liquid EDLCs. (3) The total contribution of the anion is greater than that of the cation, which indicates that the charging contribution of each ion species need not be the same. $[EMIM]^+$ ion is slower than $[SCN]^-$ ion due to its larger size and heavy molecular weight. Combining these results, we find out that the rearrangement of the ion itself plays an important role in charging of the ionic liquid-based EDLC. Thus, when designing the EDLC with good performance, it is necessary to consider the properties of bulk ionic liquids, especially the ion mobility.

3.4.5 Discharging dynamics

As with the charging process of the EDLC, we also examined the discharging dynamics by switching the electrode potential $\Delta\Psi$ from finite values to zero. Figure 3.15 (a) compares the electrode charge during charging and discharging processes. Similar to the charging process, discharging of the EDLC shows fast dynamics; most of the electrode charges relax within 2 ns. In order to extract the timescale of the discharging processes, the electrode charges are fitted with the stretched exponential function as follows,

$$\sigma(t) = \sigma_{t=0}\exp(-(t/\tau_\alpha)^\beta), \tag{3.29}$$

where τ_α and β are fitting parameters. The relaxation times of the discharging processes from several potential conditions are depicted in the Figure 3.15 (b). The discharging time is slightly shorter than the charging times at

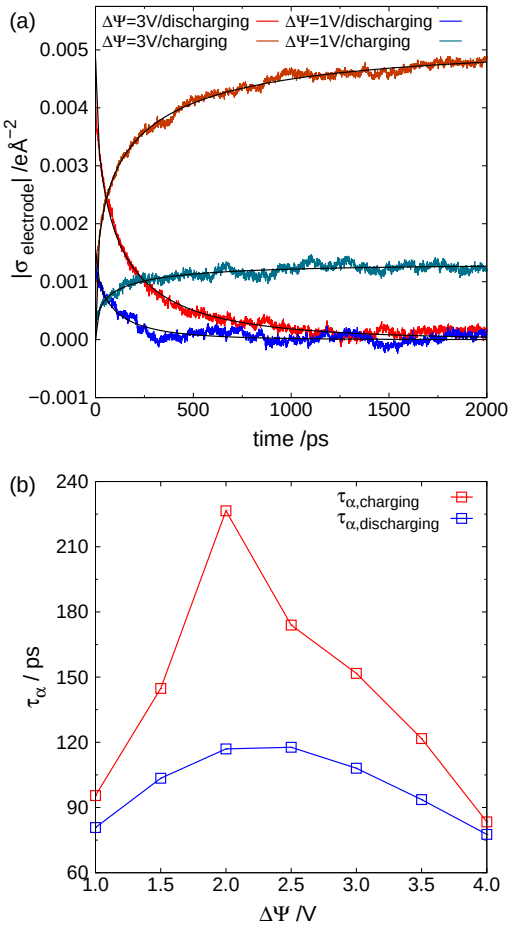

Figure 3.15: (a) The charge density of the electrode when charging/discharging. Black solid lines are fitted curves with the stretched exponential function. (b) The charging/discharging time of the EDLC as a function of $\Delta\Psi$. Blue and red lines respectively denote the τ_α of discharging and charging processes.

overall potential conditions. In a discharged state, cations and anions are adjacent to each other to maximize the stability of the Coulomb interaction. On the other hand, cations and anions form alternating layers in a charged state, as depicted in Figure 3.4. Therefore, the discharging process exhibits faster dynamics than charging because the ions in the initial state experiences the repulsive force with the adjacent co-ions.

The discharging and charging dynamics of the EDLC in our system are almost symmetric. Even though the discharging dynamics is faster than the charging dynamics, the order of the timescales are the same. In addition, the discharging dynamics also exhibits the slowest when the EDLC is discharging from the $\Delta\Psi = 2$ V condition, similar to the charging dynamics. The (dis)charging of the EDLC is induced by the rearrangement of the ionic layers, and ions near a flat electrode can rearrange their structure without a severe constraint, so the charging and discharging mechanisms are not significantly different from each other. That is, the discharging process can be understood as an inverse process of the charging process. However, a recent charging simulation in the nanoporous electrode revealed that charging and discharging dynamics are asymmetric.[103] The charging of ionic liquids in the sub-nanoporous electrode occurs with an initial condensation of the total ion density followed by the co-ion expulsion, but discharging is induced by the ion swapping. This result implies that the steric constraint of the ions near the electrode can change the charging mechanism of the EDLC. Therefore, it is necessary to study the charging mechanism for a variety of different electrode structures in the future.

3.4.6 Experimental relevance

The formation of the EDL in our system shows remarkably fast dynamics with a timescale of 1 ns. The charging and discharging processes of the ionic liquid EDLC are not induced by the diffusion of specific ions but a rearrangement of the overall ionic structure. During the rearrangement of the ionic layer, the average perpendicular displacement of each ion is within 1 Å, which is shorter than the size of the ion itself. Therefore, the EDL of ionic liquids can be rapidly formed by the rotation of ions or the cooperative motion with the adjacent ions without translation over long distances. The fast charging dynamics of the ionic liquid EDL suggests the possibility of the EDLC with high power density. However, the EDLC of the ionic liquid implemented in experiments does not show a fast charging dynamics as suggested in our study.[65] In our study, the distance between the electrodes is three to four times smaller than in typical experiments, and this may lead to a significantly faster dynamics of the EDLC. Therefore, the timescale calculated in our study can be regarded as a lower limit of the charging times of the EDLC.

Another reason for the gap between our findings and other experimental results is the electrode structure. In typical EDLC experiments, nanoporous electrodes are used to increase the energy density,[38] but the electrode in our system has a simple flat geometry. Recent studies revealed that the ruggedness and the curvature of the electrode may affect the differential capacitance of the EDLC.[44,104] In addition, the transfer of ions becomes slower under nanoconfinement condition,[105,106] which indicates that the power density of the ionic liquid EDLC can be reduced by the nanoporous

electrode geometry. Nevertheless, recent studies have shown that ionic liquids in nanopores are not always slower, rather they may exhibit faster dynamics within nanopores of optimal sizes.[107,108] Thus, if nanopores of the electrode are well designed for ionic liquids, it is expected to realize the ionic liquid EDLC with high charging rates as described in our study.

3.5 Conclusions

In summary, the structure and charging dynamics of an EDLC system, consisting of graphene and $[EMIM]^+[SCN]^-$, were studied using MD simulations. To describe the dynamics of the system accurately, the fluctuation of the electrode charge was considered by applying the constant potential simulation. It was confirmed that the correlation between the electrode charge and the adjacent ion is important in the ionic liquid-based EDLC. The ionic layer was described in terms of the orientation of the constituent ions as well as the distance from the electrodes. In the discharged state, both $[EMIM]^+$ and $[SCN]^-$ ions formed layer structures parallel to the electrodes, and the layer with such a directionality was maintained over three layers. If the electrode is charged, the ions near the electrode do not merely translate, but perform rotational motions as well, so that the ionic layers are completely rearranged. The rearrangement of the ion layer is not limited to the electrode surface but occurs over a long range scale.

The non-equilibrium charging simulations in the present study provided the molecular insight to understand the charging mechanism of the EDLC with ionic liquid electrolytes. The charging process shows a multiple time scale dynamics across the time scale corresponding to the diffusive motion

of the ion and the rearrangement of the ionic layers, so the charging of the EDLC follows the heterogeneous dynamics. Especially, the charge accumulated on the electrodes during the charging process can be quantified by the perpendicular displacement of the ions. From the displacement of ions, the contribution of each ion to the electrode charge was directly calculated. In the electric double layer adjacent to the parallel electrode, the desorption of the co-ion is more pronounced than the counter-ion adsorption, which is named vacating effect. In addition, the interfacial ionic layer alone cannot completely screen the electrode charge, so bulk state ions play an important role in the electrical performance of the EDLC. The formation of the electric double layer is induced by the collective motion of overall ions. Therefore, the displacement of each ion during the charging process is shorter than its ion size, and the EDLC shows a remarkably fast charging dynamics.

We conclude by providing our rationale that the non-equilibrium charging dynamics of the EDLC can reveal the behavior of the differential capacitance of the EDLC. Our study revealed that the differential capacitance of the EDLC and its ionic layer structure are closely related to each other. The vacating effect and the ion exchange between ionic layers, which are identified as key phenomena in determining the behavior of differential capacitance, were revealed through the non-equilibrium charging study. In addition, the non-equilibrium simulation has the advantage of directly observing the motion of ions according to the potential difference changes, which is impossible in equilibrium studies. In particular, a strong correlation between the slowest charging dynamics and the maximum differential capacitance suggests that the differential capacitance of the EDLC can be predicted by non-equilibrium charging dynamics of the EDLC.

Chapter 4. Transition Metal Dichalcogenide

Chapter 4

Transition Metal Dichalcogenide

4.1 Introduction

Transition metal dichalcogenides (TMDCs) are two-dimensional molecular layers which are weekly stacked by van der Waals attraction. Two-dimensional materials have been focused on various area because of its high surface area relative to its volume. As the first discovered 2D material, the graphene has many benefits such as high electron mobility, chemical and physical stability, but it cannot be solely applied as the electronic materials due to its semi-metallic band structure.[109] On the other hand, the TMDC is considered to be a promising 2D layer material because of its tunable band structure and interesting properties.[110–112] A TMDC layer has a three-layer structure composed of two chalcogenide layers and one transition metal layer between them. Due to the combination of the transition metal and chalcogenides, there are plenty species of TMDCs, such as MoS_2, $PtSe_2$, WS_2, WTe_2, etc. Among various TMDCs, MoS_2 has been used as electronic materials after discovering a phenomenon with a direct bandgap

of 1.9 eV in a monolayer.[112,113] In recent years, TMDC has been utilized not only as a semiconductor material but also as catalysts or adsorbents by utilizing the reactivity of the edge of TMDC layers.[114,115] Accordingly, in order to maximize edge exposure, methods of synthesizing TMDCs in the vertical direction instead of the basal plane direction are also have been developed.[110,116] However, the mechanism for determining the direction of TMDC in synthesis has not yet been clarified, and fundamental research is needed. Also, research on the electrical and chemical properties of TMDC according to morphology should be accompanied.

The present Chapter covers three topics about the TMDC as follows. Firstly, the behaviors of the MoS_2 layers under mechanical strains are investigated using non-equilibrium MD simulations. From the simulations, the chemical vapor deposition (CVD) growth mechanism of the vertically-synthesized TMDC layers is suggested. Next, the electronic band structures of the $PtSe_2$ in various morphologies were calculated via DFT method. Finally, the adsorption energy of water molecules according to the morphology of MoS_2 was calculated. These consecutive computational studies provide new insights on better understanding the TMDC's growth principles and their applications. The remainder of the present Chapter is organized as follows. section 4.2 is devoted to introducing a brief overview related to the TMDCs. Models and calculating methods are explained in section 4.3. Corresponding calculation results and discussions are presented in section 4.4. Concluding remarks are given at section 4.5.

4.2 Overview of TMDC

4.2.1 Structure and properties of TMDC

Each TMDC layer consists of three layers, two layers of the chalcogenides and one layer of transition metal between them. Thus, it has a chemical formula MX_2, where M and X denote the transition metal and the chalcogenides, respectively. Generally, each TMDC layer can have two kinds of phase, 2H and 1T phases, depending on the relative lateral position of chalcogenides. In the 2H phase, lateral positions of two chalcogenide layers are coincident with each other following the stacking order of *ABA*. On the other hand, the stacking order of the 1T phase TMDC follows the *ABC* form, as depicted in Figure 4.1. The relative stability between the two phases is dependent on the combination of a transition metal and a chalcogenide. As the chalcogenide increases, there is a tendency that the 1T phase becomes more stable.[117] For example, the 2H phase is more stable in MoS_2 and WS_2, while the 1T phase is more stable in WTe_2 and $PtSe_2$. The phase of the TMDC does not only affect the stability but also the electronic band structure of the TMDC, *e.g.* the electronic band structure of MoS_2 follows metallic behavior in the 1T phase, but it has a semiconductor band structure in the 2H phase.

In addition to the phase of each TMDC layer itself, the morphology of TMDC layers is also important for the properties of the TMDC. The bandgap of the TMDC is affected by the number of layers on which the layers are stacked. Due to the easily manipulating bandgap of the TMDC, it has been used as electronic materials such as transistors and electrodes.[110,118] Among various TMDCs, bulk MoS_2 has an indirect bandgap of 1.3 eV, but

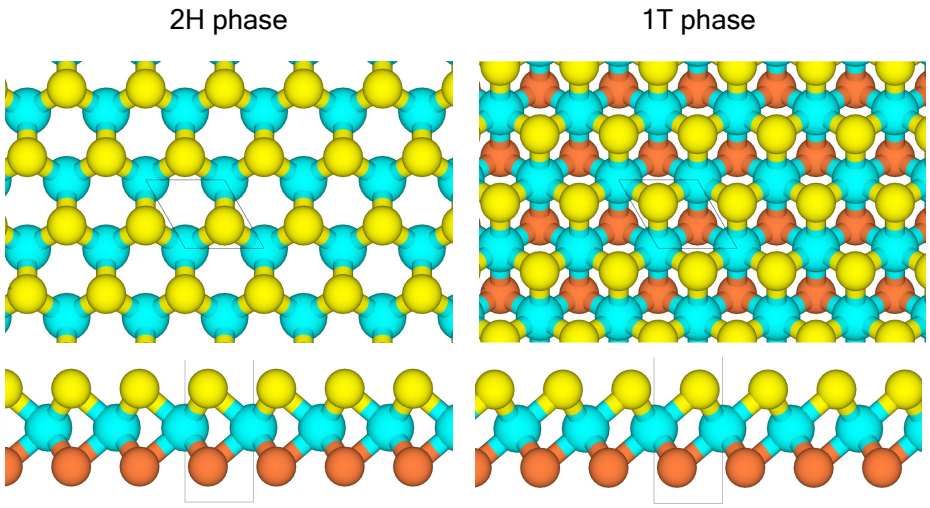

Figure 4.1: 2H and 1T phases of the TMDC. Cyan spheres denote transition metal atoms, and yellow and orange spheres denote chalcogenide atoms. The color of chalcogenide atoms is differentiated for each layer in order that the layers can be easily distinguished.

the bandgap of the monolayer transits to a direct bandgap of 1.8 eV. The direct bandgap of the MoS_2 monolayer induces the photoluminescence, which opens the potential of many optoelectronic applications.[113] The aforementioned electronic properties are based on the structure of the intact basal plane of the TMDC layer. On the other hand, by utilizing the edge of the TMDC layer having high chemical reactivity, TMDC layers have been used as adsorbents or chemical catalysts.[114,115] That is, the chemical reactivity of TMDC can be improved by adjusting the orientation of the TMDC to increase the exposure ratio of the edges.

4.2.2 Synthesis of TMDC

The 2D TMDC layers can be synthesized in both top-down and bottom-up methods. The earliest monolayers of TMDCs were synthesized by a mechanical exfoliation, a method of peeling layers from a bulk crystal one by one with an adhesive tape.[119] Another method of synthesizing the TMDC layer is the chemical exfoliation in which the layers are separated from bulk TMDC crystals through a lithium intercalation or a sonication.[120] The mechanical and chemical exfoliations are advantageous in that the layer can be obtained in simple processes if only crystals can be prepared. However, these exfoliation methods have some limitations common in most top-down methods: (1) It is difficult to synthesize a uniform, large-scale layer in industrial scale. (2) Defects are generated in TMDC layers during the synthesis process. (3) It is difficult to synthesize TMDC of various phases and morphology.

As an alternative to overcome the aforementioned deficiencies, the CVD method has been developed to synthesize the various TMDCs of high quality. CVD is a method to synthesize semiconductors by injecting precursor molecules in a high-temperature gas form on the metal substrate, which acts as a catalyst. Because of the good reactivity of the CVD process, there are various strategies to synthesize TMDC layers. For example, the MoS_2 layers, which is the most popular TMDC, can be synthesized in following ways: (1) Directly evaporation of MoS_2 powder on a solid substrate at high temperature produces small flakes of single-layer MoS_2.[121] (2) Evaporation of both molybdenum and sulfur precursors on a metallic substrate in a vacuum chamber produces discontinuous films.[122] (3) Evaporation of volatile

MoO_3 on a solid substrate followed by sulfurization effectively grows triangularly shaped uniform MoS_2 monolayers.[123] (4) Direct sulfurization of a pre-deposited thin molybdenum film on a substrate produces continuous large-scale 2D MoS_2 layers, as depicted in Figure 4.2.[116,124] As presented in various methods for producing TMDCs, CVD method is highly sensitive to the experimental condition, such as temperature, a flow rate of gas, and thickness of the precursors. Especially, by increasing the initial thickness of the pre-deposited Mo films, the orientation of the MoS_2 can be regulated.[116]

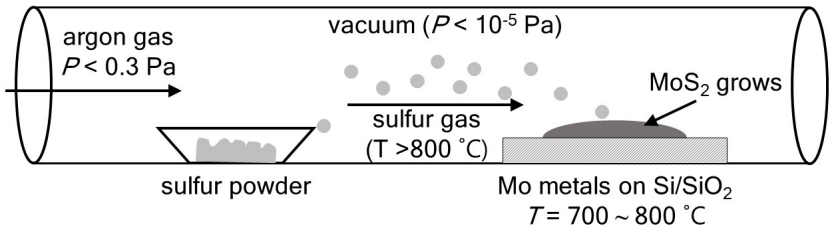

Figure 4.2: A schematic figure in which MoS_2 is synthesized by sulfurization of pre-deposited Mo films.

4.3 Models and Methods

4.3.1 Straining MD simulations for MoS_2

In order to investigate the microscopic origin on experimental observations that the growth direction of MoS_2 layers depends on the thickness of the Mo seed film, we performed MD simulations. All MD simulations were per-

formed using the LAMMPS package.[91] The initial configurations of 2H-phase 2D MoS_2 layers were generated using the force-field parameters, and they were relaxed at 300 K using Nosé-Hoover chain method, implementing canonical ensemble. After a short relaxation period, strain was applied to the layers by decreasing the periodic box size along the armchair direction at a strain rate of $1 \times 10^8 \sim 1 \times 10^9$ s^{-1} at every time step, which was set to be 0.2 fs. During the simulation, a periodic boundary condition was applied to xyz direction, and vacuum was inserted in perpendicular to lateral direction to reduce the effect of periodic images. The interaction of MoS_2 was described using a ReaxFF forcefield,[125] which is an empirical forcefield describing the bond-breaking and forming events. The ReaxFF parameters for MoS_2 have been adopted to describe the various mechanical properties of 2D MoS_2 layers.[126–128]

4.3.2 Band structure of TMDC

In order to investigate the transition of electronic structure of the $PtSe_2$ of various morphology, we carried out Ab initio calculation based on density functional theory (DFT) calculation with Vienna ab initio simulation package (VASP).[30] Here, the wave functions were approximated with the projector augmented wave (PAW) pseudo-potentials.[31] The exchange-correlation functional was described by generalized gradient approximation (GGA) of the Perdew-Burke-Ernzerhof (PBE) parameter.[23,24] A cutoff energy of 500 eV was used and the geometry optimization was performed until the energy convergence satisfies the 1.0×10^{-5} eV/Å. In the case of the bulk $PtSe_2$, the unit cell, as well as the atomic positions, were relaxed during the geometry optimization, and the rest $PtSe_2$ layer structures were relaxed

while the unit cell is fixed. The unit cell of the pristine $PtSe_2$ is set to be the hexagonal lattice, but that of the vertical $PtSe_2$ is the orthorhombic lattice. We checked that the shape of the unit cell does not affect the projected density of the states (PDOS). During the calculation, the first Brillouin zone was sampled with the Monkhorst-Pack grid of $11 \times 11 \times 11$ k points for the monolayer and bulk pristine $PtSe_2$ layers and $7 \times 7 \times 3$ k points for vertically aligned $PtSe_2$ structures.

4.3.3 Water adsorption on MoS_2 layers

In order to calculate the adsorption energy of a water molecule on MoS_2 layers in various morphology, DFT calculations were conducted using Vienna ab initio simulation package (VASP).[30] Interactions between electrons and nuclei are represented by the projector augmented wave (PAW) pseudopotentials with generalized gradient approximation (GGA) of the Perdew-Burke-Ernzerhof (PBE) formulation.[23,24,31] Brillouin zone was sampled using a Monkhorst-Pack grid of $7 \times 7 \times 3$ k points, and a cutoff energy of 400 eV was used. In addition, DFT-d3 correction was applied to account for the van der Waals interactions.[25] Vacuum regions larger than 10 Å were imposed between MoS_2 layers to avoid the artificial interactions between periodic images.

4.4 Results and Discussions

4.4.1 Growth of MoS_2 in CVD

As introduced in section 4.2, the uniform MoS_2 can be synthesized in large scale through CVD method in which pre-deposited Mo films are sulfurized.[116] Interestingly, the synthesized MoS_2 layers are dependent on the thickness of pre-deposited Mo films. If the Mo film thickness is less than 5 nm, the synthesized MoS_2 layers are aligned parallel to the substrate, but the layers are perpendicularly aligned when the thickness is larger than that. The process of synthesizing the MoS_2 through the CVD can be explained as follows. Throughout sulfurization, 2D MoS_2 layers grow in the layer-by-layer manner accompanying a substantive volumetric expansion, *i.e.*, conversion of Mo to MoS_2. At the initial stage, horizontal expansion of MoS_2 is not prevented by adjacent layers and proceeds without accumulating significant strain due to the large free volume between the Mo nanoparticles. However, as the free volume decreases due to the continued growth of MoS_2, the MoS_2 layer experiences a lateral strain with the adjacent layers.

To investigate the exclusive role of the strain energy in determining 2D layer growth mode, we performed MD simulations using ReaxFF potential, an empirical force-field that can describe bond-breaking and forming.[125,129] Since it is technically challenging to entirely simulate the growth event of two-dimensional MoS_2 layers with identical experimental conditions, we performed non-equilibrium MD simulations by introducing protocols to mimic the strain imposed by the sulfurization of molybdenum. We first identified how pristine 2D MoS_2 in the form of single and multilayers rearrange their structures under lateral strain. Figure 4.3 compares the morphologies of 2D

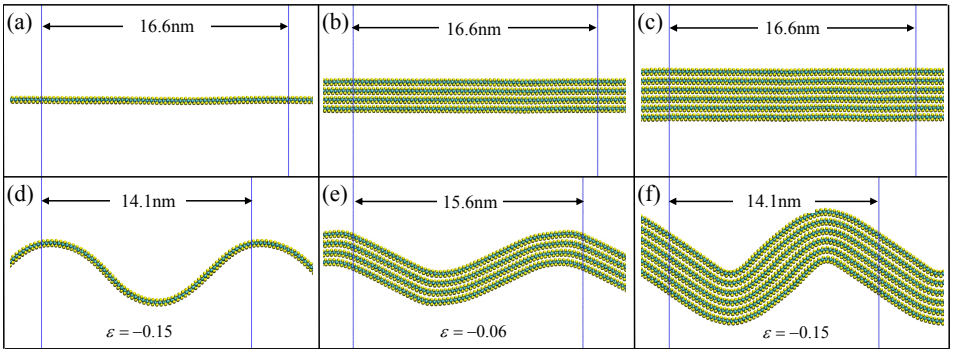

Figure 4.3: Configurations of MoS_2 layers during compression. neat (a) monolayer, (b) quadlayer, (c) hexalayer, and compressed (d) monolayer, (e) quadlayer, (f) hexalayer.

MoS_2 layers in pristine states (top panels) and under lateral strain (bottom panels). Consistent with previous experiments and calculations,[130,131] 2D MoS_2 layers can bear a large degree of mechanical flexibility/bendability under lateral strain. This finding indicates that deformed 2D MoS_2 multilayers do not suffer from the weakening of van der Waals interaction across their basal planes once they are formed. Accordingly, they are not easily separable under externally exerted lateral strain, but rearrange their layer orientations. In addition, deformed 2D MoS_2 layers possess energy penalties of several hundred kcal per mole compared to the horizontal 2D layers in pristine states. This trend becomes more pronounced with increasing physical confinement against the rearrangement of 2D MoS_2 layers such as when they are grown from Mo nanoparticles of high densities.

In Figure 4.4, MD simulations were performed by exerting lateral strain to two MoS_2 quadlayers, which describes their initial growth stage in the

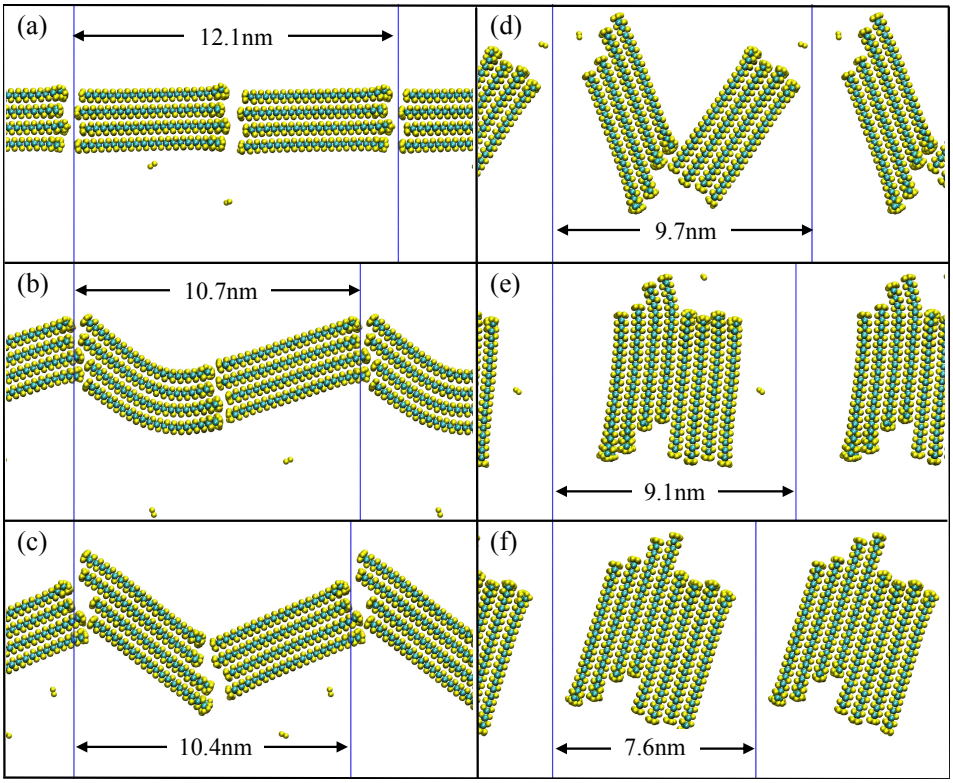

Figure 4.4: Configurations of two MoS_2 quadlayers during compression

physically confined environment. Upon increasing lateral strain, the 2D MoS_2 layers initially in a horizontal orientation start to readjust their layer orientations to relieve the exerted strain. Due to the intrinsically high flexibility of the MoS_2 layers, they can easily bend while maintaining interlayer vdW bonds. Upon continued strain, the layers reach a certain curvature limit by being pushed together and rotate along the direction perpendicular to the initial orientation. As a result, two MoS_2 quadlayers stick together to

form one bundle of vertically oriented octalayers. The Figure 4.6 illustrates the MD simulation results performed for 2D MoS_2 layers of larger layer numbers, describing the structural rearrangement of horizontal 2D MoS_2 octalayers upon increasing strain. Although the layers do not completely rotate in the vertical orientation, they prefer to be realigned perpendicular to the direction of the exerted strain forming obliquely oriented layers.

To compare the growth characteristics of 2D MoS_2 layers under conditions of low physical confinement, mimicking the condition of thin Mo thickness condition, we also simulated the structural configuration of isolated horizontal monolayers under lateral strain (Figure 4.5). Once the initially separated two monolayers impinge upon each other, they become slightly deflected to relieve the strain accompanying the slip of one layer on the other rather than rotating layer orientations. Subsequently, they form horizontally oriented bi-layers and this event continuously happens on the numerous nucleation sites filling the free volume in between them. As a result,

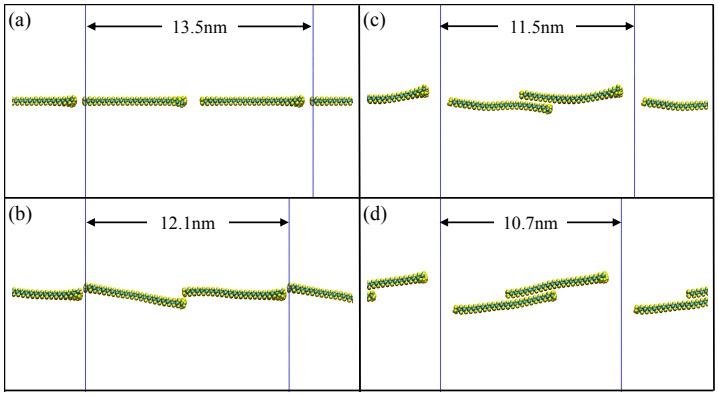

Figure 4.5: Configurations of two MoS_2 monolayers during compression

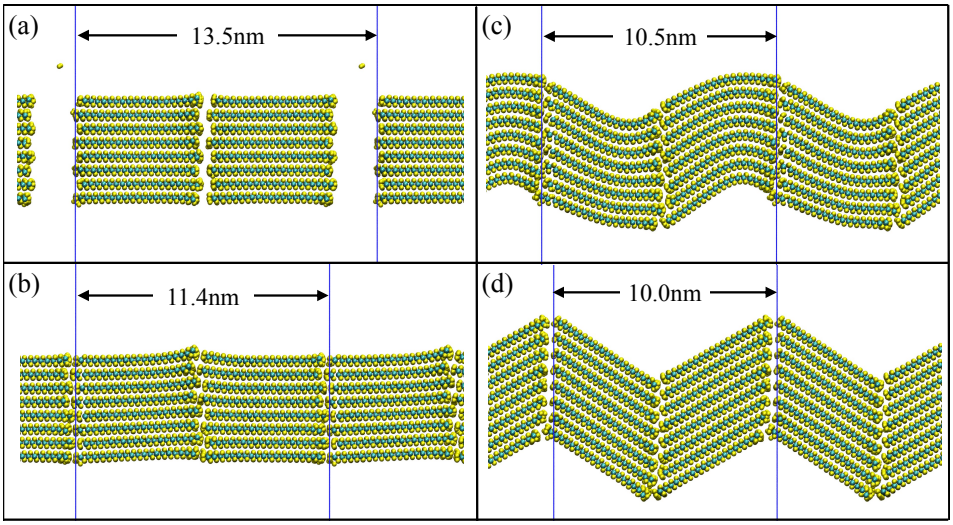

Figure 4.6: Configurations of two MoS_2 quadlayers during compression

horizontally oriented 2D MoS_2 multilayers are grown. Combining these non-equilibrium simulation results, the internal strain developed during growth of MoS_2 dictates the orientation of MoS_2 layers.

Figure 4.7 summarizes the mechanism of the TMDC growth from the pre-deposited metals of different thickness. Figure 4.7 (a) describes the growth situation when thin Mo is sulfurized on the substrate. Mo films of such a small thickness consist of Mo nanoparticles with large free volume in between them. During sulfurization, 2D MoS_2 layers grow in the layer-by-layer manner accompanying a substantive volumetric expansion. Because of large free volume, the 2D layers are able to grow filling in the free volume without readjusting layer orientations, which results in horizontally-aligned TMDC layers. On the other hand, the growth of MoS_2 layers from thick

Mo films suffer a different situation, as depicted in Figure 4.7 (b). Such a thick Mo film consists of continuously connected Mo nanoparticles and lacks free volume. Thus, the volume expansion through the conversion from Mo to MoS_2 is accompanied by a significant accumulation of lateral strains. Accordingly, continuously growing 2D layers are forced to reorient their structures in a way to release the strain, which results in vertically-aligned MoS_2 layers.

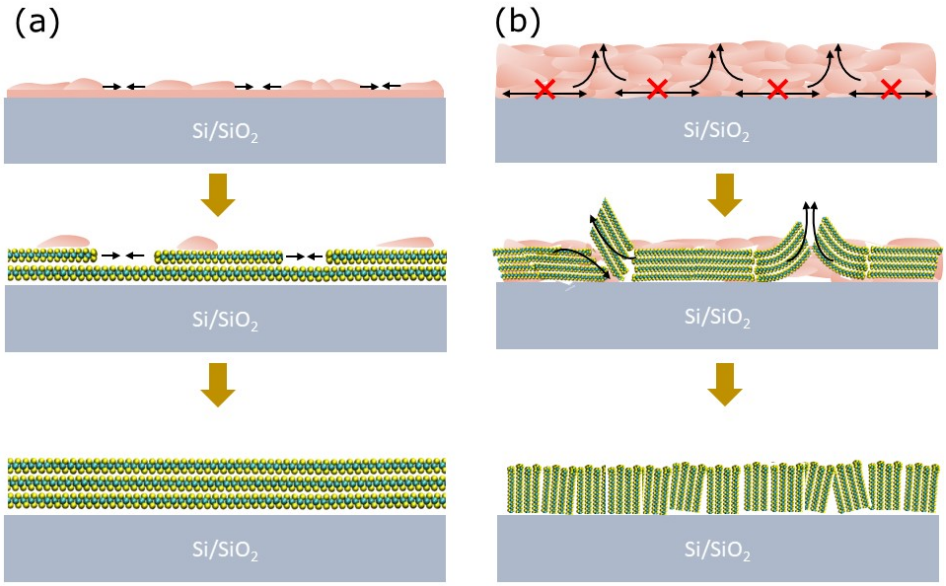

Figure 4.7: Schematics for the TMDC growth from pre-deposited metal films of different thickness. (a) Layer-by-layer growth of horizontal 2D MoS_2 layers from thin Mo films on the substrate (b) Vertically reoriented 2D MoS2 layers on the substrate, achieved by sulfurizing thick Mo.

4.4.2 Band structure of TMDC

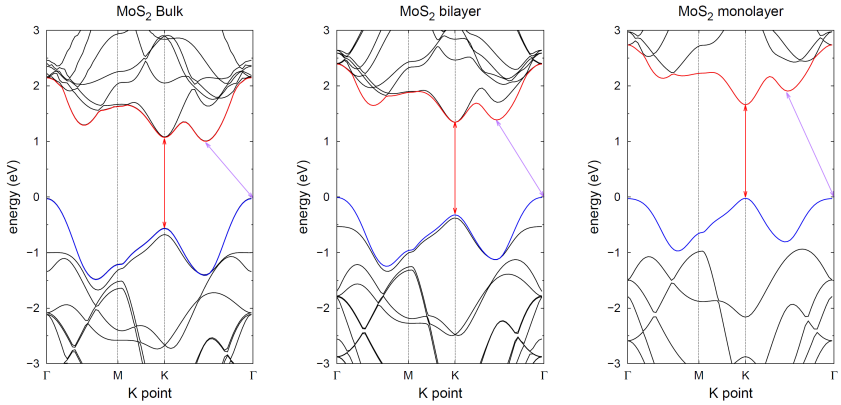

Figure 4.8: Electronic band structures of MoS_2 bulk, bilayer and monolayer structures. The unit cell of the MoS_2 is the hexagonal lattice. Band structure is scanned along $\Gamma - M - K - \Gamma$ lines.

In this section, we investigated the electronic band structure of TMDC layers in various morphology. We first demonstrated the method described in section 4.3.2 by reproducing the transition of the band structure when morphology of MoS_2 changes from bulk to monolayer phase. Figure 4.8 shows the consecutive band structure of the bulk, bilayer, and monolayer of the MoS_2. The bulk phase of MoS_2 has a direct gap at K point and an indirect gap from Γ point to the point between K and Γ points. The estimated band gap of the direct and indirect gaps are 1.8 eV and 1.3 eV, respectively, which indicates that the bulk phase of MoS_2 has a fundamental indirect transition. However, when the number of MoS_2 layers decreases becoming a monolayer, the energy of the valence band at the Γ point decreases, so the

direct gap of 1.8 eV at the K point becomes a fundamental gap. These band structures of MoS_2 layers are consistent with the experimental results.[113]

In order to clarify the mechanism for the transition of carrier transport properties of $PtSe_2$, we calculated the electronic structures of the 2D $PtSe_2$ of various layer morphology and orientations. From our calculation condition, the lattice constant of the $PtSe_2$ is determined as 3.78 Å and the thickness of each layer is optimized as 2.58 Å. The distance between $PtSe_2$ layers in bulk phase is determined as 5.12 Å. Figure 4.9(a) shows the projected density of states (PDOS) and the band structures of 2D $PtSe_2$ layers calculated along the $K-\Gamma-M-K$ points in the hexagonal Brillouin zone. The band gap of the $PtSe_2$ monolayer is determined as 1.3 eV, but the bulk state of $PtSe_2$ shows metallic band structure, consistent with the previously reported band structures.[132] In addition to the horizontally-aligned $PtSe_2$ layers, the electronic structure of vertically-aligned $PtSe_2$ layers was calculated along the $\Gamma - X - S - Y - \Gamma - Z - U - R - T - Z$ points in the orthorhombic Brillouin zone (Figure 4.9 (b)-(d)). Vertically-aligned 2D $PtSe_2$ layers of various vertical lengths were modeled, i.e., 7.9 Å, 10 Å, and 20 Å corresponding to Figure 4.9 (b)-(d) respectively, along with the fixed interlayer spacing of 5.12 Å. Although the band structures become highly complicated with the increasing number of atoms within the unit cells, all the vertically-aligned 2D $PtSe_2$ layers exhibit zero bandgap energies irrespective of their vertical lengths. It is noteworthy that the zero gap band behavior shows even when the $PtSe_2$ length is shorter than the 8 Å. We also studied how the edge configuration of vertically-aligned 2D PtSe2 layers affects their band structures by altering the number of exposed Se atoms on their vertical edges. In addition to Figure 4.9 (b)-(d) where each 2D layer

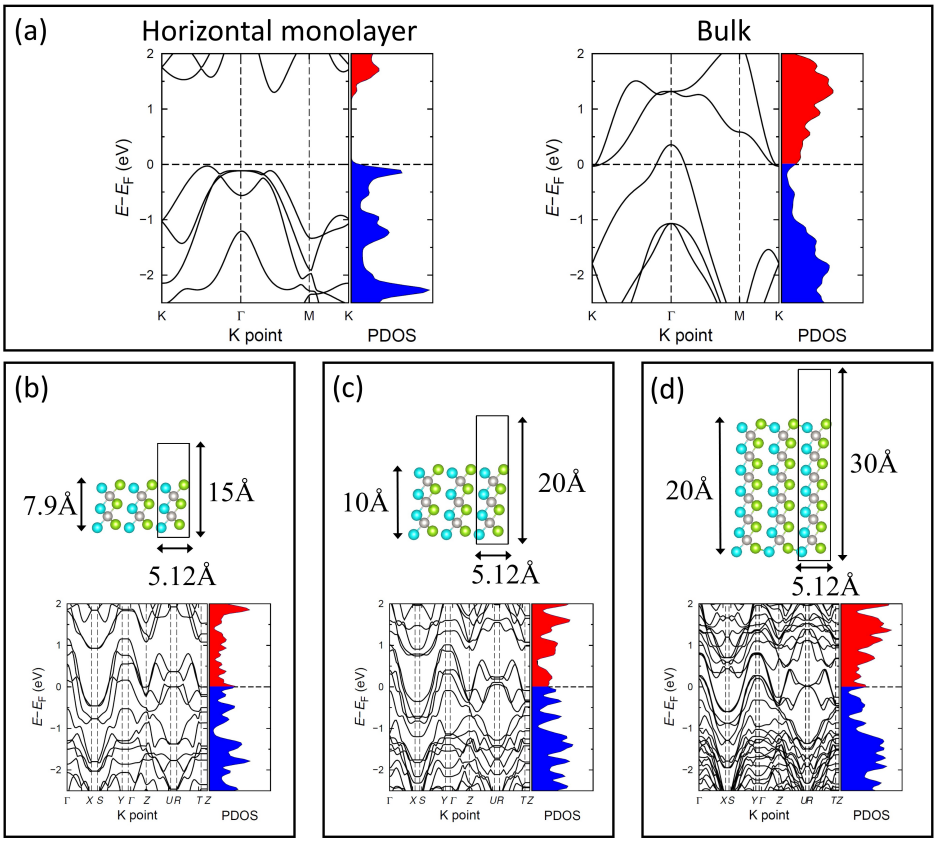

Figure 4.9: Electronic band structures and projected density of states (PDOS) of $PtSe_2$ for (a) 2D monolayer vs. bulk. (b-d) Vertically-aligned 2D layers of various layer lengths (b) 7.9 Å. (c) 10 Å. (d) 20 Å. A vacuum of $\sim$ 10 Å was inserted between the vertical $PtSe_2$ layers.

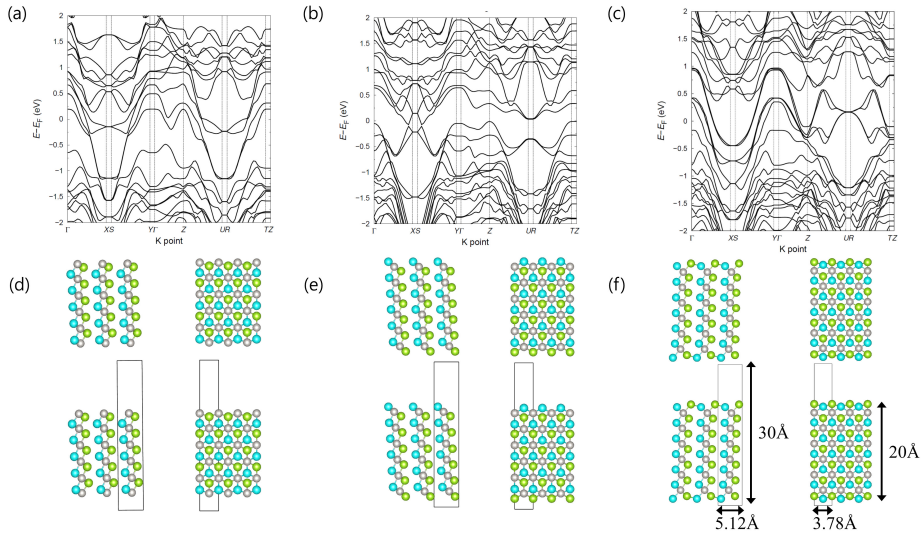

Figure 4.10: Band structures of vertically-aligned $PtSe_2$ layers with various edge states.

edge contains two Se atoms, we also calculated the band structure of vertical 2D $PtSe_2$ layers when one Se and one Pt atoms are exposed on their edges, as depicted in Figure 4.10. Although the band structures slightly vary depending on their edge configuration, it is commonly observed that vertically-aligned 2D $PtSe_2$ layers show metallic carrier transports with zero bandgap energies. All these comprehensive results strongly confirm the transition of semiconducting-to-metallic carrier transports as the orientation of 2D $PtSe_2$ layers transit from horizontal to vertical. Moreover, they indicate that the bandgap energies of 2D $PtSe_2$ layers are mainly determined by the number of stacked 2D layer basal planes.

4.4.3 Water adsorption on MoS_2 layers

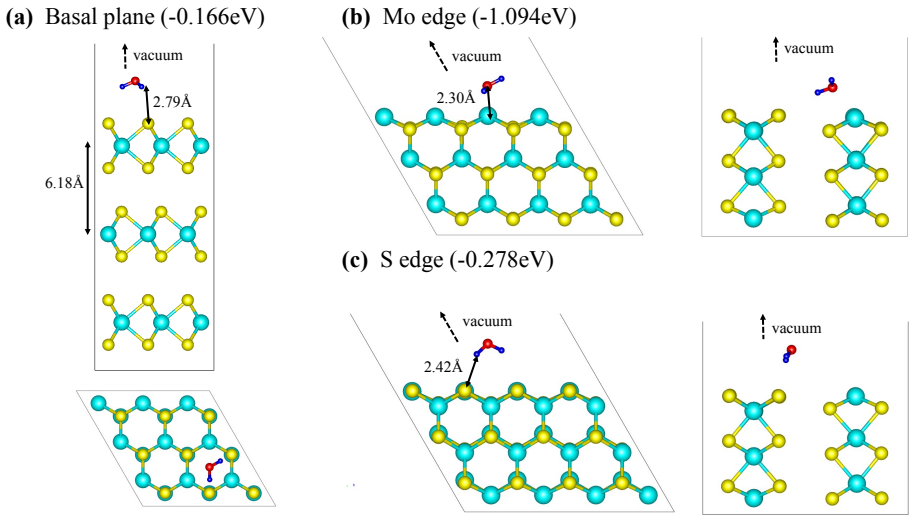

Figure 4.11: Structure of water molecules on the MoS_2 layers, and the corresponding adsorption energies.

In this section, in order to quantitatively verify how the orientation of two-dimensional MoS_2 layers affects the sensitivity to vaporized water, we calculated the adsorption energies of water molecules with varying layer orientation. The DFT calculation results confirm that water molecules are more strongly adsorbed onto the edge sites than the basal planes of 2D MoS_2 layers; the adsorption energy of one water molecule on the basal plane is calculated to be 0.166 eV while those on the Mo and S edges are 1.094 eV and 0.278 eV, respectively. The adsorption energy, E_{ads}, of a water molecule on 2D MoS_2 layers was calculated as $E_{\text{ads}} = E_{\text{tot}} - (E_{MoS_2} + E_{\text{water}})$, where

E_{tot} is the energy of 2D MoS_2 layers with an adsorbed water molecule, and E_{MoS_2} and E_{water} are the energies of 2D MoS_2 layers and a water molecule, respectively. The much larger adsorption energy on the Mo edge over the S edge is because Mo, a transition metal, is more prone to form additional atomic bonds over S. This claim is supported by the schematic illustration in Figure 4.11 (c) which depicts that the oxygen of a water molecule is directed to the exposed Mo edge opposite to the case of the S edge (Figure 4.11 (b)). Although all 2D MoS_2 layer edges do not expose Mo sites only, it is evident that vertically-aligned 2D MoS_2 layers exhibit significantly enriched dangling bonds compared to horizontal 2D layers, which guarantees improved reactivity upon water molecule adsorption.

4.5 Conclusions

In this Chapter, we investigated the mechanism of determining the orientation of TMDC layers during CVD synthesis and the effect of the morphology of TMDC layer on their electronic and chemical properties. First, we simulated the synthesis process of 2D MoS_2 layers through non-equilibrium MD simulations applying an external strain to the MoS_2 layers. Van der Waals bonding between stacked MoS_2 layers is strong enough that the multilayer TMDC is not separated by the strain exerted in the direction of the basal plane. Thus, at the initial stage of the synthesis, the TMDC layer is formed into horizontally oriented multilayers. However, the free volume between the TMDC layers decreases as the synthesis continues, and the growing TMDC multilayers push each other and become mechanically deformed. To release this exerted strain, the TMDC layers are rotated perpendicu-

larly with respect to the initially aligned orientation. That is, the TMDC layers are synthesized in a direction perpendicular to the substrate due to the mechanical strain during the CVD synthesis. In addition, we also investigated the electronic and chemical reactivity of TMDCs according to their morphologies using DFT method. $PtSe_2$ has an electronic structure of a semiconductor in a single layer, but has a metallic property in a bulk state. The vertically aligned $PtSe_2$ has a metal electronic structure similar to the bulk phase. In addition, the band gap structure did not change much in the edge structure or length of the layer. In other words, the bandgap structures of the TMDC are strongly influenced by the number of stacked layers. Finally, we revealed that the chemical reactivity of the vertically-aligned TMDC is largely enhanced by the dangling atoms of the edge of the TMDC layers. These results provide new insights to better understand the properties of TMDCs and their applications.

Bibliography

[1] Kim, Y.; Shin, S.; Kang, H. *Angewandte Chemie International Edition* **2015**, *54*, 7626–7630.

[2] Wagner, F. T.; Moylan, T. E. *Surface Science* **1988**, *206*, 187 – 202.

[3] Mezger, M.; Schröder, H.; Reichert, H.; Schramm, S.; Okasinski, J. S.; Schöder, S.; Honkimäki, V.; Deutsch, M.; Ocko, B. M.; Ralston, J.; Rohwerder, M.; Stratmann, M.; Dosch, H. *Science* **2008**, *322*, 424–428.

[4] Mezger, M.; Schramm, S.; Schröder, H.; Reichert, H.; Deutsch, M.; De Souza, E. J.; Okasinski, J. S.; Ocko, B. M.; Honkimäki, V.; Dosch, H. *The Journal of Chemical Physics* **2009**, *131*, 094701.

[5] Black, J. M.; Walters, D.; Labuda, A.; Feng, G.; Hillesheim, P. C.; Dai, S.; Cummings, P. T.; Kalinin, S. V.; Proksch, R.; Balke, N. *Nano Letters* **2013**, *13*, 5954–5960.

[6] Jurado, L. A.; Espinosa-Marzal, R. M. *Scientific Reports* **2017**, *7*, 4225.

[7] SALAPAKA, S. M.; SALAPAKA, M. V. *IEEE Control Systems Magazine* **2008**, *28*, 65–83.

[8] Hahn, J. R.; Lee, C. W.; Han, S.-J.; Lahaye, R. J. W. E.; Kang, H. *The Journal of Physical Chemistry A* **2002**, *106*, 9827–9831.

[9] Trenary, M. *Annual Review of Physical Chemistry* **2000**, *51*, 381–403.

[10] Kim, Y.; Noh, C.; Jung, Y.; Kang, H. *Chemistry –A European Journal* **2017**, *23*, 17566–17575.

[11] Schmickler, W.; Santos, E. *Interfacial electrochemistry*; Springer Berlin Heidelberg, 2010; pp 1–272.

[12] Chan, K.; Nørskov, J. K. *The Journal of Physical Chemistry Letters* **2016**, *7*, 1686–1690.

[13] Skulason, E.; Karlberg, G. S.; Rossmeisl, J.; Bligaard, T.; Greeley, J.; Jónsson, H.; Nørskov, J. K. *Phys. Chem. Chem. Phys.* **2007**, *9*, 3241–3250.

[14] Seh, Z. W.; Kibsgaard, J.; Dickens, C. F.; Chorkendorff, I.; Nørskov, J. K.; Jaramillo, T. F. *Science* **2017**, *355*, eaad4998.

[15] Quaino, P.; Luque, N.; Soldano, G.; Nazmutdinov, R.; Santos, E.; Roman, T.; Lundin, A.; Groth, A.; Schmickler, W. *Electrochimica Acta* **2013**, *105*, 248 – 253.

[16] Santos, E.; Quaino, P.; Schmickler, W. *Phys. Chem. Chem. Phys.* **2012**, *14*, 11224–11233.

[17] Wilhelm, F.; Schmickler, W.; Nazmutdinov, R. R.; Spohr, E. *The Journal of Physical Chemistry C* **2008**, *112*, 10814–10826.

[18] Roman, T.; Groß, A. *Catalysis Today* **2013**, *202*, 183 – 190.

[19] Wilhelm, F.; Schmickler, W.; Spohr, E. *Journal of Physics: Condensed Matter* **2010**, *22*, 175001.

[20] Schmickler, W.; Wilhelm, F.; Spohr, E. *Electrochimica Acta* **2013**, *101*, 341 – 346.

[21] VandeVondele, J.; Krack, M.; Mohamed, F.; Parrinello, M.; Chassaing, T.; Hutter, J. *Computer Physics Communications* **2005**, *167*, 103 – 128.

[22] Hutter, J.; Iannuzzi, M.; Schiffmann, F.; VandeVondele, J. *Wiley Interdisciplinary Reviews: Computational Molecular Science* **2014**, *4*, 15–25.

[23] Perdew, J. P.; Burke, K.; Ernzerhof, M. *Phys. Rev. Lett.* **1996**, *77*, 3865–3868.

[24] Perdew, J. P.; Burke, K.; Ernzerhof, M. *Phys. Rev. Lett.* **1997**, *78*, 1396–1396.

[25] Grimme, S.; Antony, J.; Ehrlich, S.; Krieg, H. *The Journal of Chemical Physics* **2010**, *132*, 154104.

[26] Byrd, R.; Lu, P.; Nocedal, J.; Zhu, C. *SIAM Journal on Scientific Computing* **1995**, *16*, 1190–1208.

[27] Schmidt, M. W.; Baldridge, K. K.; Boatz, J. A.; Elbert, S. T.; Gordon, M. S.; Jensen, J. H.; Koseki, S.; Matsunaga, N.; Nguyen, K. A.; Su, S.; Windus, T. L.; Dupuis, M.; Montgomery, J. A. *Journal of Computational Chemistry* **1993**, *14*, 1347–1363.

[28] Becke, A. D. *Phys. Rev. A* **1988**, *38*, 3098–3100.

[29] Lee, C.; Yang, W.; Parr, R. G. *Phys. Rev. B* **1988**, *37*, 785–789.

[30] Kresse, G.; Furthmüller, J. *Phys. Rev. B* **1996**, *54*, 11169–11186.

[31] Kresse, G.; Joubert, D. *Phys. Rev. B* **1999**, *59*, 1758–1775.

[32] Lackey, D.; Schott, J.; Sass, J.; Woo, S.; Wagner, F. *Chemical Physics Letters* **1991**, *184*, 277 – 281.

[33] Lechner, B. A. J.; Kim, Y.; Feibelman, P. J.; Henkelman, G.; Kang, H.; Salmeron, M. *The Journal of Physical Chemistry C* **2015**, *119*, 23052–23058.

[34] Nie, S.; Feibelman, P. J.; Bartelt, N. C.; Thürmer, K. *Phys. Rev. Lett.* **2010**, *105*, 026102.

[35] Zimbitas, G.; Haq, S.; Hodgson, A. *The Journal of Chemical Physics* **2005**, *123*, 174701.

[36] Kang, H. *Accounts of Chemical Research* **2005**, *38*, 893–900.

[37] Burt, R.; Birkett, G.; Zhao, X. S. *Phys Chem Chem Phys* **2014**, *16*, 6519–6538.

[38] González, A.; Goikolea, E.; Barrena, J. A.; Mysyk, R. *Renewable and Sustainable Energy Reviews* **2016**, *58*, 1189 – 1206.

[39] Park, S. W.; DeYoung, A. D.; Dhumal, N. R.; Shim, Y.; Kim, H. J.; Jung, Y. *J Phys Chem Lett* **2016**, *7*, 1180–1186.

[40] Islam, M. M.; Alam, M. T.; Okajima, T.; Ohsaka, T. *Journal of Physical Chemistry C* **2009**, *113*, 3386–3389.

[41] Liu, X. H.; Wang, Y. Y.; Li, S.; Yan, T. Y. *Electrochimica Acta* **2015**, *184*, 164–170.

[42] Kornyshev, A. A. *Journal of Physical Chemistry B* **2007**, *111*, 5545–5557.

[43] Feng, G.; Huang, J.; Sumpter, B. G.; Meunier, V.; Qiao, R. *Phys Chem Chem Phys* **2011**, *13*, 14723–14734.

[44] Hu, Z. Z.; Vatamanu, J.; Borodin, O.; Bedrov, D. *Electrochimica Acta* **2014**, *145*, 40–52.

[45] Vatamanu, J.; Vatamanu, M.; Borodin, O.; Bedrov, D. *J Phys Condens Matter* **2016**, *28*, 464002.

[46] Lauw, Y.; Horne, M. D.; Rodopoulos, T.; Nelson, A.; Leermakers, F. A. M. *Journal of Physical Chemistry B* **2010**, *114*, 11149–11154.

[47] Shim, Y.; Kim, H. J.; Jung, Y. *Faraday Discuss.* **2012**, *154*, 249–263.

[48] Shim, Y.; Jung, Y.; Kim, H. J. *The Journal of Physical Chemistry C* **2011**, *115*, 23574–23583.

[49] Vatamanu, J.; Bedrov, D. *The Journal of Physical Chemistry Letters* **2015**, *6*, 3594–3609, PMID: 26722729.

[50] Fedorov, M. V.; Kornyshev, A. A. *Chemical Reviews* **2014**, *114*, 2978–3036.

[51] Chmiola, J.; Yushin, G.; Gogotsi, Y.; Portet, C.; Simon, P.; Taberna, P. L. *Science* **2006**, *313*, 1760–1763.

[52] Kondrat, S.; Kornyshev, C.; Pérez, V.; Presser, Y.; Gogotsi, A. *Energy and Environmental Science* **2012**, *5*, 6474–6479.

[53] Brownson, D. A.; Kampouris, D. K.; Banks, C. E. *Journal of Power Sources* **2011**, *196*, 4873–4885.

[54] Huang, X.; Zeng, Z.; Fan, Z.; Liu, J.; Zhang, H. *Advanced Materials* **2012**, *24*, 5979–6004.

[55] Chen, Y.; Zhang, X.; Zhang, D.; Yu, P.; Ma, Y. *Carbon* **2011**, *49*, 573–580.

[56] Tsai, W.-Y.; Lin, R.; Murali, S.; Li Zhang, L.; Mcdonough, J. K.; Ruoff, R. S.; Taberna, P.-L.; Gogotsi, Y.; Simon, P. *Nano Energy* **2012**, *2*, 403–411.

[57] Jo, S.; Park, S.-W.; Shim, Y.; Jung, Y. *Electrochimica Acta* **2017**, *247*, 634 – 645.

[58] Jo, S.; Park, S.-W.; Noh, C.; Jung, Y. *Electrochimica Acta* **2018**, *284*, 577 – 586.

[59] DeYoung, A. D.; Park, S. W.; Dhumal, N. R.; Shim, Y.; Jung, Y.; Kim, H. J. *Journal of Physical Chemistry C* **2014**, *118*, 18472–18480.

[60] Mahurin, S. M.; Surwade, S. P.; Crespo, M.; Dai, S. *Journal of Raman Spectroscopy* **2016**, *47*, 585–590.

[61] Thangavel, R.; Kannan, A. G.; Ponraj, R.; Thangavel, V.; Kim, D.-W.; Lee, Y.-S. *Journal of Power Sources* **2018**, *383*, 102 – 109.

[62] Lockett, V.; Horne, M.; Sedev, R.; Rodopoulos, T.; Ralston, J. *Phys Chem Chem Phys* **2010**, *12*, 12499–12512.

[63] Lockett, V.; Sedev, R.; Ralston, J.; Horne, M.; Rodopoulos, T. *Journal of Physical Chemistry C* **2008**, *112*, 7486–7495.

[64] Sun, G.-H.; Li, K.-X.; Sun, C.-G. *Journal of Power Sources* **2006**, *162*, 1444–1450.

[65] Zhong, C.; Deng, Y.; Hu, W.; Qiao, J.; Zhang, L.; Zhang, J. *Chemical Society Reviews* **2015**, *44*, 7484–7539.

[66] Helmholtz, H. *Annalen der Physik* **1879**, *243*, 337–382.

[67] Brown, M.; Abbas, Z.; Kleibert, A.; Green, R.; Goel, A.; May, S.; Squires, T. *Physical Review X* **2016**, *6*, 011007.

[68] Bazant, M. Z.; Storey, B. D.; Kornyshev, A. A. *Phys Rev Lett* **2011**, *106*, 046102.

[69] Goodwin, Z. A.; Feng, G.; Kornyshev, A. A. *Electrochimica Acta* **2017**, *225*, 190 – 197.

[70] Limmer, D. T. *Phys. Rev. Lett.* **2015**, *115*, 256102.

[71] Griffin, J. M.; Forse, A. C.; Tsai, W.-Y.; Taberna, P.-L.; Simon, P.; Grey, C. P. *Nature Materials* **2015**, *14*, 812 – 820.

[72] Kirchner, K.; Kirchner, T.; Ivaništšev, V.; Fedorov, M. *Electrochimica Acta* **2013**, *110*, 762–771.

[73] Vatamanu, J.; Borodin, O.; Bedrov, D.; Smith, G. D. *The Journal of Physical Chemistry C* **2012**, *116*, 7940–7951.

[74] Fedorov, M. V.; Kornyshev, A. A. *Electrochimica Acta* **2008**, *53*, 6835–6840.

[75] Fedorov, M. V.; Georgi, N.; Kornyshev, A. A. *Electrochemistry Communications* **2010**, *12*, 296–299.

[76] Limmer, D. T.; Salanne, M.; van Roij, R.; Madden, P. A.; Chandler, D.; Rotenberg, B. *The Journal of Physical Chemistry C* **2014**, *118*, 18291–18298.

[77] Xu, K.; Ji, X.; Zhang, B.; Chen, C.; Ruan, Y.; Miao, L.; Jiang, J. *Electrochimica Acta* **2016**, *196*, 75–83.

[78] Jiang, X.; Huang, J.; Zhao, H.; Sumpter, B. G.; Qiao, R. *Journal of Physics: Condensed Matter* **2014**, *26*, 284109.

[79] Kong, X.; Lu, D.; Liu, Z.; Wu, J. *Nano Research* **2015**, *8*, 931–940.

[80] Péan, C.; Merlet, C.; Rotenberg, B.; Madden, P. A.; Taberna, P.-L.; Daffos, B.; Salanne, M.; Simon, P. *ACS Nano* **2014**, *8*, 1576–1583.

[81] Endres, F.; MacFarlane, D.; Abbott., A. *Electrodeposition from ionic liquids*; Wiley-VCH: Weinheim, 2008; p 26.

[82] Gouy, M. *J. Phys. Theor. Appl.* **1910**, *9*, 457–468.

[83] Chapman, D. L. *The London, Edinburgh, and Dublin Philosophical Magazine and Journal of Science* **1913**, *25*, 475–481.

[84] Stern, O. *Zeitschrift fïr Elektrochemie und angewandte physikalische Chemie 30*, 508–516.

[85] Reed, S. K.; Lanning, O. J.; Madden, P. A. *The Journal of Chemical Physics* **2007**, *126*, 084704.

[86] Wang, Z.; Yang, Y.; Olmsted, D. L.; Asta, M.; Laird, B. B. *The Journal of Chemical Physics* **2014**, *141*, 184102.

[87] Canongia Lopes, J. N.; Deschamps, J.; Pádua, A. A. H. *The Journal of Physical Chemistry B* **2004**, *108*, 2038–2047.

[88] Canongia Lopes, J. N.; Deschamps, J.; Pádua, A. A. H. *The Journal of Physical Chemistry B* **2004**, *108*, 11250–11250.

[89] Dhungana, K. B.; Faria, L. F. O.; Wu, B.; Liang, M.; Ribeiro, M. C. C.; Margulis, C. J.; Castner, E. W. *The Journal of Chemical Physics* **2016**, *145*, 024503.

[90] Hummer, G.; Rasaiah, J. C.; Noworyta, J. P. *Nature* **2001**, *414*, 188–190.

[91] Plimpton, S. *Journal of Computational Physics* **1995**, *117*, 1 – 19.

[92] Yeh, I.-C.; Berkowitz, M. L. *The Journal of Chemical Physics* **1999**, *111*, 3155–3162.

[93] Hockney, R. W. *Computer simulation using particles / R.W. Hockney and J.W. Eastwood.*, special student ed.. ed.; Taylor & Francis, 1988.

[94] Vatamanu, J.; Borodin, O.; Smith, G. D. *Journal of the American Chemical Society* **2010**, *132*, 14825–14833.

[95] Feng, G.; Zhang, J. S.; Qiao, R. *Journal of Physical Chemistry C* **2009**, *113*, 4549–4559.

[96] Merlet, C.; Salanne, M.; Rotenberg, B.; Madden, P. A. *The Journal of Physical Chemistry C* **2011**, *115*, 16613–16618.

[97] Tazi, S.; Salanne, M.; Simon, C.; Tury, P.; Pounds, M.; Madden, P. A. *Journal of Physical Chemistry B* **2010**, *114*, 8453–8459.

[98] Park, S.-W. Heterogeneous dynamics and electrolyte applications of ionic liquids. Ph.D. thesis, Seoul National University, Seoul, Korea, 2016.

[99] Park, S.-W.; Kim, S.; Jung, Y. *Phys. Chem. Chem. Phys.* **2015**, *17*, 29281–29292.

[100] Kim, S.; Park, S.-W.; Jung, Y. *Phys. Chem. Chem. Phys.* **2016**, *18*, 6486–6497.

[101] Kim, D.; Jeong, D.; Jung, Y. *Phys. Chem. Chem. Phys.* **2014**, *16*, 19712–19719.

[102] Reichert, P.; Kjær, K. S.; Brandt van Driel, T.; Mars, J.; Ochsmann, J. W.; Pontoni, D.; Deutsch, M.; Nielsen, M. M.; Mezger, M. *Faraday Discuss.* **2018**, *206*, 141–157.

[103] Vatamanu, J.; Borodin, O.; Olguin, M.; Yushin, G.; Bedrov, D. *Journal of Materials Chemistry A* **2017**, *5*, 21049–21076.

[104] Ma, K.; Woodward, C. E.; Forsman, J. *The Journal of Physical Chemistry C* **2014**, *118*, 15825–15834.

[105] Perkin, S. *Phys. Chem. Chem. Phys.* **2012**, *14*, 5052–5062.

[106] Monk, J.; Singh, R.; Hung, F. R. *The Journal of Physical Chemistry C* **2011**, *115*, 3034–3042.

[107] Iacob, C.; Sangoro, J. R.; Kipnusu, W. K.; Valiullin, R.; Kärger, J.; Kremer, F. *Soft Matter* **2012**, *8*, 289–293.

[108] He, Y.; Qiao, R.; Vatamanu, J.; Borodin, O.; Bedrov, D.; Huang, J.; Sumpter, B. G. *The Journal of Physical Chemistry Letters* **2016**, *7*, 36–42.

[109] Geim, A. K. *Science* **2009**, *324*, 1530–1534.

[110] Hu, Z.; Wu, Z.; Han, C.; He, J.; Ni, Z.; Chen, W. *Chemical Society Reviews* **2018**, *47*, 3100–3128.

[111] Song, I.; Park, C.; Choi, H. C. *RSC Advances* **2015**, *5*, 7495–7514.

[112] Chhowalla, M.; Shin, H. S.; Eda, G.; Li, L.-J.; Loh, K. P.; Zhang, H. *Nature Chemistry* **2013**, *5*, 263.

[113] Splendiani, A.; Sun, L.; Zhang, Y.; Li, T.; Kim, J.; Chim, C.-Y.; Galli, G.; Wang, F. *Nano Letters* **2010**, *10*, 1271–1275.

[114] Wang, H.; Lu, Z.; Xu, S.; Kong, D.; Cha, J. J.; Zheng, G.; Hsu, P.-C.; Yan, K.; Bradshaw, D.; Prinz, F. B.; Cui, Y. *Proceedings of the National Academy of Sciences* **2013**, *110*, 19701–19706.

[115] Cho, S.-Y.; Kim, S. J.; Lee, Y.; Kim, J.-S.; Jung, W.-B.; Yoo, H.-W.; Kim, J.; Jung, H.-T. *ACS Nano* **2015**, *9*, 9314–9321.

[116] Jung, Y.; Shen, J.; Liu, Y.; Woods, J. M.; Sun, Y.; Cha, J. J. *Nano letters* **2014**, *14*, 464.

[117] Duerloo, K.-A.; Li, Y.; Reed, E. *Nature Communications* **2014**, *5*.

[118] Podzorov, V.; Gershenson, M. E.; Kloc, C.; Zeis, R.; Bucher, E. *Applied Physics Letters* **2004**, *84*, 3301–3303.

[119] Novoselov, K. S.; Jiang, D.; Schedin, F.; Booth, T. J.; Khotkevich, V. V.; Morozov, S. V.; Geim, A. K. *Proceedings of the National Academy of Sciences of the United States of America* **2005**, *102*.

[120] Matte, H. S. S. R.; Gomathi, A.; Manna, A. K.; Late, D. J.; Datta, R.; Pati, S. K.; Rao, C. N. R. *Angew. Chem. Int. Ed. Engl.* **2010**, *49*, 4059–4062.

[121] Wu, S.; Huang, C.; Aivazian, G.; Ross, J. S.; Cobden, D. H.; Xu, X. *ACS nano* **2013**, *7*, 2768–2772.

[122] Helveg,; Lauritsen,; Laegsgaard,; Stensgaard,; Nørskov,; Clausen,; Topsoe,; Besenbacher, *Physical review letters* **2000**, *84*, 951–954.

[123] Lee, Y.; Zhang, X.; Zhang, W.; Chang, M.; Lin, C.; Chang, K.; Yu, Y.; Wang, J. T.; Chang, C.; Li, L.; Lin, T. *Advanced Materials* **2012**, *24*, 2320–2325.

[124] Kong, D.; Wang, H.; Cha, J. J.; Pasta, M.; Koski, K. J.; Yao, J.; Cui, Y. *Nano letters* **2013**, *13*, 1341–1347.

[125] Chenoweth, K.; van Duin, A. C. T.; Goddard, W. A. *The Journal of Physical Chemistry A* **2008**, *112*, 1040–1053.

[126] Ostadhossein, A.; Rahnamoun, A.; Wang, Y.; Zhao, P.; Zhang, S.; Crespi, V. H.; van Duin, A. C. T. *The journal of physical chemistry letters* **2017**, *8*, 631–640.

[127] Mortazavi, B.; Ostadhossein, A.; Rabczuk, T.; van Duin, A. C. T. *Phys. Chem. Chem. Phys.* **2016**, *18*, 23695–23701.

[128] Shi, Y.; Cai, Z.; Pu, J.; Wang, L.; Xue, Q. *Ceramics International* **2018**, *45*, 2258–2265.

[129] Senftle, T. P.; Hong, S.; Islam, M. M.; Kylasa, S. B.; Zheng, Y.; Shin, Y. K.; Junkermeier, C.; Engel-Herbert, R.; Janik, M. J.; Aktulga, H. M.; Verstraelen, T.; Grama, A.; van Duin, A. C. T. *Npj Computational Materials* **2016**, *2*, 15011.

[130] Wang, P.; Xiao, S.; Li, X.; Lyu, B.; Huang, Y.; Cheng, S.; Huang, H.; He, J.; Gao, Y. *Scientific Reports* **2015**, *5*, 18441.

[131] Jiang, J. W. *Nanotechnology* **2014**, *25*, 355402.

[132] Wang, Y. et al. *Nano Letters* **2015**, *15*, 4013–4018.

국문초록

본 학위 논문에서는 다양한 계면에 대해 분자 동역학과 밀도범함수 이론을 활용한 전산모사 연구를 수행하였다. 계면은 상이 다른 두 물질이 인접한 영역으로써 실질적인 화학 반응이 일어나는 영역이다. 물질의 크기가 작아질수록 계면의 역할이 커지게 되므로 물질의 미시적인 성질을 이해하기 위해서는 필수적으로 연구해야 하는 영역이다. 그러나 계면에 대한 실험적인 연구는 기술적인 한계로 인해 제약되는 상황이 많기 때문에 전산모사를 통해 이를 보완할 수 있다. 본 학위 논문에서는 계면의 역할이 중요해지는 다음의 세 종류의 계에 대해 연구를 수행하였다. (1) 백금 표면에서의 하이드로늄 이온, (2) 전기이중층 축전기, (3) 2차원 전이금속 다이찰코제나이드.

첫번째 챕터에서는 백금(111) 표면에서의 하이드로늄 이온의 구조 및 에너지에 대해 밀도범함수 이론을 활용하여 연구를 수행했다. 하이드로늄 이온은 이웃한 물 분자와 다중 결합된 상태로 백금 표면에 흡착될 수 있다. 금속 표면에서 하이드로늄 이온의 안정성을 결정하는 가장 중요한 물리량은 금속의 일함수라는 점을 밝혀냈다. 또한, 금속에 직접적으로 흡착된 양성자는 물 분자가 추가되면 수소결합 사이의 양성자 호핑 움직임을 통해 벌크 상태로 이동할 수 있다. 이 결과를 종합하여 수소 원자가 하이드로늄으로 이온화되는 Volmer 반응이 두단계에 걸쳐서 일어나며, 금속 결합된 하이드로늄 이온은 중간체로서 전기화학에서 중요한 역할을 한다는 점을 밝혀냈다.

두번째 챕터에서는 분자동역학 방법론을 통해 1-에틸-3-페틸이미다졸륨 싸이오싸이아네이트 ($[EMIM]^+[SCN]^-$) 이온성 액체가 전해질로 이용된 전기이중층 축전기의 충전 현상을 연구했다. 이온층 구조로부터 미분 전기용량을 계산하였고, 전기용량이 최대값을 갖는 전압 조건에서 이온층의 구조가 급격히 변한다는 점을 밝혀냈다. 축전기의 충전 과정을 직접적으로 모사하는 비평형 시뮬레이션을 통해 전극의 충전 동역학도 이온층의 구조의 변화에 크게 의존한다는 점을 밝혀냈다. 특히, 충전 과정 중에 전극 전하의 변화량은 이온성 액체 분자의 수직 변위와 일치한다. 이를 통해, 각 이온 분자별로 충전에 미치는 기여도를 분석하였다. 전극의 충전은 반대 이온의 흡착보다는 공동이온의 탈착에 크게 의존한다. 또한, 축전기의 전극 계면 이온층뿐만 아니라 벌크 영역의 이온층 역시 충전 과정에 큰 역할을 한다는 점을 밝혀냈다.

마지막 챕터에서는 이차원 전이금속 다이칼코게나이드의 방향과 물성에 대한 연구를 수행했다. 먼저, 화학 기상 증착법에 의해 합성되는 MoS_2의 방향이 사전 증착된 몰리브데늄의 두께에 의해 조절되는 성장 메커니즘을 비평형 분자동역학 시뮬레이션을 통해 연구하였다. 시뮬레이션 결과를 통해 합성되는 이차원 MoS_2층의 방향성은 성장 중에 발생하는 내부 변형에 기인한다는 것을 밝혀냈다. 다음으로, 다양한 형태의 전이금속 다이칼코게나이드 층의 전자 밴드 구조를 계산하였다. 전이금속 다이칼코게나이드의 밴드갭 구조는 층의 가장자리나 층의 길이보다는 겹쳐있는 층 수에 크게 의존한다는 점을 밝혔다. 마지막으로, 물 분자가 MoS_2의 가장자리에 매달려 있는 원자와 쉽게 결합할 수 있다는 것을 밝혀냈다. 이 연구를 통해 이차원 전이금속 다이칼코게나이드 층의 다양한 형태와 그 응용 방법에 대한 새로운 관점을 제공할 수 있었다.

주요어: 계면, 하이드로늄 이온, 백금 표면, 이온성 액체, 전기이중층, 전기이중층 축전기, 전이금속 다이칼코게나이드, 밀도범함수 이론, 분자 동역학

학번: 2011-20292